PDF hosted at the Radboud Repository of the Radboud University Nijmegen

Phase transitions reflected in HF-EPR spectra

Een wetenschappelijke proeve op het gebied
van de Natuurwetenschappen,
Wiskunde en Informatica.

Proefschrift

ter verkrijging van de graad van doctor
aan de Radboud Universiteit Nijmegen,
op gezag van de Rector Magnificus prof. dr. C.W.P.M. Blom,
volgens het besluit van het College van Decanen
in het openbaar te verdedigen op 31 oktober 2006
des namiddags om 3:30 precies

door
Eric van der Horst

geboren op 21 juni 1974
te Amsterdam

Promotor : Prof. dr. ir. J.C. Maan

Co-Promotor : Dr. P.J.M. van Bentum

Manuscriptcommissie : Prof. dr. A. Kentgens (vz)

Dr. E.J. Reijerse
Max Plank Institute for Bioinorganic Chemistry, Germany

Dr. O. Wittlin
Polish Academy of Sciences, Poland

Voor Laura

Voorwoord

What is the sound of one hand clapping? ...

Een AIO, zonder klankbord, medewerking en collega's kan geen proefschrift schrijven. Een van de moeilijkste onderdelen van een proefschrift is dan ook het dankwoord. Als eerste bedank ik mijn vrouw. Laura, het moet voor jou niet altijd makkelijk geweest zijn dat ik zo veel van huis was om mijn experimenten te doen. Niet alleen overdag maar ook 's nachts en in de weekenden. Ik hoop dat de afronding van dit "project" een en ander goedmaakt. Ik dank je in ieder geval voor je geduld, begrip en gezond verstand als ik weer eens overdreef met de uren die ik op het lab doorbracht.

De tweede persoon die ik veel verschuldigd ben is mijn dagelijks begeleider. Jan, het moet zwaar voor je geweest zijn om een in proza gespecialiseerde gas-fase chemicus om te scholen tot een experimentele vaste stof fysicus. Buiten jouw praktische vaardigheden, improvisatie vermogen en vakkundig geschreven simulatie- en meetsoftware ben je ook een goede steun geweest in moeilijke tijden en in het beteugelen van mijn al te wilde ideeën. Tevens wist je me steeds weer te motiveren als de experimenten of de uitwerkingen tegenzaten en ik kan dan ook stellig zeggen dat zonder jou dit proefschrift niet in deze vorm zou zijn verschenen.

Voor mijn kennismaking met zowel de apparatuur waarmee ik in deze periode heb gewerkt als met de goede dingen van het leven, en dan met name het cabaret, ben ik Marc veel dank verschuldigd, hoewel ik nooit zijn voorliefde voor waterfietsen ben gaan delen. Voor een diepere kennismaking met Nijmegen ben ik mijn kamergenoten van het eerste uur dank verschuldigd, Sjoerd en Alex, herzlichen Dank.

De overige A/OIO's, hoofdvak studenten en vaste stafleden die hebben meegewerkt om mijn tijd in Nijmegen leuk en productief te maken noem ik hieronder in willekeurige volgorde omdat de lijst anders te lang wordt. De beoordeling aan de bijdrage kan een ieder zelf invullen, dus bedankt Freddy, Maaike Cecile, Urs, Kostya, Igor, Fausto, Ate, Andrea, Marius, Cecilia, Fabio, Ken, Klaas, Maarten, Jos P.,Andre, Martha, Ine, Marijn, Louis, Adrie, Stef W., Stef O. Frans en John. Van buiten de afdeling dan nog Alex Priem, Robert Stolk, Ed Reijerse, Adri Klaassen, Fred Hagen en Paul van Kan.

Zonder de hulp van de technische staf van het magnetenlab om de apparatuur te onderhouden, of in het geval van kleinmetaal te maken, strandt ieder onderzoek al snel op de technische onkunde van de experimentator. In dat opzicht ben ik dank verschuldigd aan Jos R., Lijnis, Harrie en Henk. Speciale dank gaat naar Hung, voor zijn hulp (inclusief baby-sitten) bij de magnetisatie metingen van hoofdstuk 4.

Reinforcements from abroad came from various countries. From beautiful Pisa came help in the form of Giuseppe Annino and Prof. Martinelli. *Mille Grazie.* From France came the hardware support for the MVNA, from the company *ABmm.* Both Phillippe and Michel, thanks for your help in getting a chemist started with the experimental hardware needed in solid state physics.

Als laatste wil ik alle leden en (gast)docenten van Dojo SUHARI (Amsterdam) bedanken voor de broodnodige ontspanning door lichaamlijke inspanning op de vrijdag avond. Van Nijmegen naar Amsterdam rijden om te trainen is niet altijd makkelijk geweest, maar het was wel altijd de moeite van de reis waard.

. . . it is the sound of no-sound.

Contents

Chapter 1

High Frequency - Electron Paramagnetic Resonance

1.1 Introduction to EPR

Electron Paramagnetic Resonance (EPR) is the process of resonant absorption of microwave radiation by paramagnetic molecules or ionic centers, containing at least one unpaired electron, in the presence of a magnetic field. EPR is used to study the interaction between electronic states and magnetic fields. E.K. Zavoisky is generally credited with the discovery of EPR spectroscopy, due to his work on the relaxation of Mn^{2+} ions in solution in the presence of a magnetic field [1].

This description immediately states the limitations faced by the EPR spectroscopist. Most (organic) systems have a closed valance shell, and hence have no unpaired electrons. The majority of EPR research is therefore dedicated to systems that have unpaired electrons and sufficiently weak magnetic interactions not to give rise to (anti)ferromagnetism. Among the traditionally most studied systems are paramagnetic ions in salts (for instance the ones described in chapters 3 and 4), the electrons in partially filled bands in both semiconductors and metals, *"rare"* stable radicals such as the oxygen bi-radical (chapter 5) and impurities in EPR silent hosts. EPR is also used to study the spin states of the metal center in biomolecules [2] and organometallic complexes.

It is a powerful technique that allows to elucidate the spin state of individual paramagnetic systems. This is contrary to a magnetization experiment that yields only information about the total magnetization from which individual properties can be determined [3]. In cases where paramagnetic domains coexist with ferro or anti-ferromagnetic domains, it becomes difficult to correlate the magnetization data to individual spins, while EPR can still yields this information, see chapter 4.

1.1.1 The *g*-value

EPR becomes a particularly relevant experiment when the magnetic spins are embedded in a crystal lattice. The spectra then reflect the magnetic interactions in solids and the coupling of magnetism to crystal field and lattice vibrations.

The simplest EPR system is a single electron in a vacuum. Due to the intrinsic magnetic moment of the electron the energy of the two levels, for the parallel or anti-parallel alignment with respect to the applied magnetic field, becomes non degenerate and dependent on the external magnetic field (fig. 1.1).

The resonance is detected when the energy difference between the two

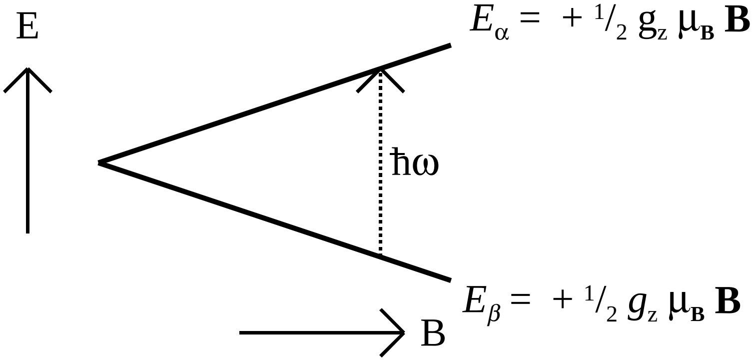

Figure 1.1: The resonance condition for a single electron in vacuum in the presence of an external magnetic field, directed along the z axis of the spin system.

spin states equals the energy of the applied photons (eq. 1.1). The ratio between magnetic field and microwave frequency, or spectroscopic splitting factor (g) is given by:

$$\Delta E = g\mu_B B_0 = \hbar\omega_0 \tag{1.1}$$

$$g = \frac{\hbar\omega_0}{\mu_B B_0} \tag{1.2}$$

Where B_0 is the field of maximum absorbance, usually determined by the zero crossing in first derivative (field modulated) spectra; μ_B is the Bohr magneton, h is Planck's constant and $\frac{\omega_0}{2\pi}$ is the microwave frequency. For an electron in vacuum $g = 2.00232\ldots$ [4].

In case the unpaired electron is surrounded by a chemical environment which is not spherically symmetric the effective g-value is dependent on the orientation of the molecule with respect to the magnetic field. Depending on the anisotropy of the g-values the effect leads to line broadening or to complete splitting of the single resonance for different orientations with respect to the magnetic field (fig. 1.2) [5].

The Zeeman term of the spin Hamiltonian depends on the spin state of the molecule, the g-tensor anisotropy and the magnetic field components along the three principle axes [5, 6, 7, 8]. The Zeeman term can be written in the generic form:

$$\mathcal{H} = \mu_B \overrightarrow{B}\overline{\overline{g}}\overrightarrow{S} \tag{1.3}$$

In which $\overrightarrow{B}$ is the static flux density, $\overline{\overline{g}}$ is a 3x3 matrix containing g_{xx}, g_{xy}, $\ldots$, g_{zz}. In cases were a principal axis system can be assigned, in which the off-diagonal terms are zero, the three principal values of the g-matrix will be expressed as g_x, g_y and g_z. $\overrightarrow{S}$ is the vector operator with the respective S$_x$, S$_y$ and S$_z$ spin operators.

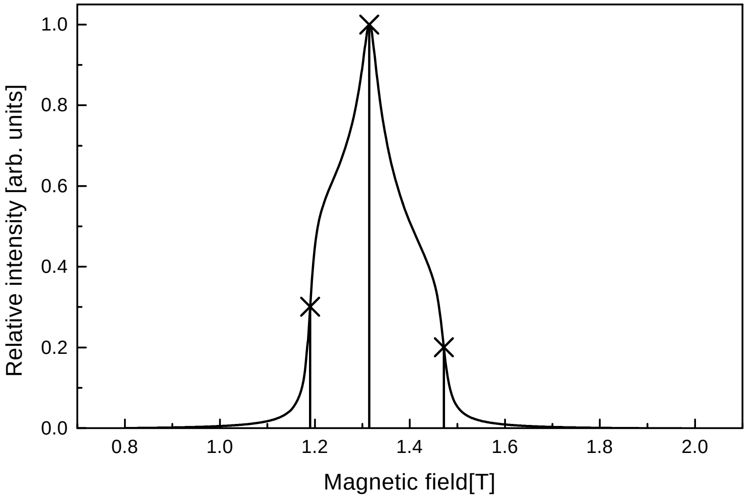

Figure 1.2: Magnetic field positions and line shape of the absorbance corresponding to an $S = \frac{1}{2}$ spin system of a crystalline powder with $g_x = 1.7$, $g_y = 1.9$ and $g_z = 2.1$ at 35 GHz.

1.1.2 Interaction with the nuclear spin

Especially at low external magnetic field, the electron paramagnetic resonance is influenced by the presence of magnetic nuclei in close proximity. Due to dipolar coupling of the nuclear spin to the electron a hyperfine pattern is detected.

The hydrogen atom is an example of a system in which this hyperfine interaction occurs due to the presence of the of the nuclear spin of the hydrogen nucleus. The general spin Hamiltonian is:

$$\mathcal{H} = \mu_B \overrightarrow{B}\overline{\overline{g}}\overrightarrow{S} - \gamma_N \hbar \overrightarrow{B}\,\overrightarrow{I} + \overrightarrow{S}\overline{\overline{A}}\overrightarrow{I} \qquad (1.4)$$

In which the first two terms are the Zeeman terms for the electron and the proton respectively, and the last is the interaction term. After reduction this leads to the following four eigenvalues (for the magnetic field parallel to the S_z direction:

Assuming the hyperfine interaction is larger than the nuclear Zeeman

$$\begin{array}{lcll} E_1 & = & & \frac{1}{2}(g\mu_B\beta - \gamma\hbar)B_0 + \frac{1}{4}a \\ E_{2,3} & = & - & \frac{1}{4}a \pm \frac{1}{2}\sqrt{a^2 + (g\mu_B + \gamma\hbar)^2 B_0^2} \\ E_4 & = & - & \frac{1}{2}(g\mu_B - \gamma\hbar)B_0 + \frac{1}{4}a \end{array}$$

splitting there are two allowed transitions, E_3 to E_1 and E_4 to E_2 ($|\beta_e\alpha_p>$ to $|\alpha_e\alpha_p>$ and $|\beta_e\beta p>$ to $|\alpha_e\beta_p>$). The energy difference between these two resonances is the nuclear hyperfine interaction. In general the hyperfine interaction is not detectable in high frequency EPR, since the line widths of the observed resonances are broader, around 0.1 T, than the hyperfine interaction, typically of the order of 10 mT.

1.1.3 Zero field splitting and rhombicity

For $S = \frac{1}{2}$ systems g-tensor anisotropy is the only effect of the environment, while for higher spin systems ($S = 1$, $\frac{3}{2}$, 2, etc) it becomes more complicated.

For example in a triplet molecule (2 unpaired electrons), if the magnetic field is increased from zero, the relative energies of the three states start to differ. If the orientation is such that the applied magnetic field direction coincides with one of the intermolecular axes, only two of the states change energy and the third remains unaffected. A different one of the three energy levels remains unaffected if the experiment is repeated along each of the molecular axis (fig. 1.3 (A)). If the crystal field is of axial (cylindrical) or lower symmetry the zero field degeneracy is lifted. A graphical representation of this symmetry is displayed for an octahedral crystal (fig. 1.3 (B)). The interaction may be represented by the addition of a term DS_z^2 to Hamiltonian 1.3. Generally a constant is added to leave the center of gravity of the spectrum unchanged [5]:

$$\mathcal{H} = \mu_B \overrightarrow{B}\overline{\overline{g}}\overrightarrow{S} + D\left(S_z^2 - \frac{S\,(S+1)}{3}\right) \tag{1.5}$$

with S the total spin of the system.

In cases where the zero field splitting axis is a rotational axis of threefold or higher symmetry, there is no difference between the remaining energy levels. At two fold symmetry such as is depicted for an octahedral symmetry (fig. 1.3 (C)), an additional term is included lifting the last zero field

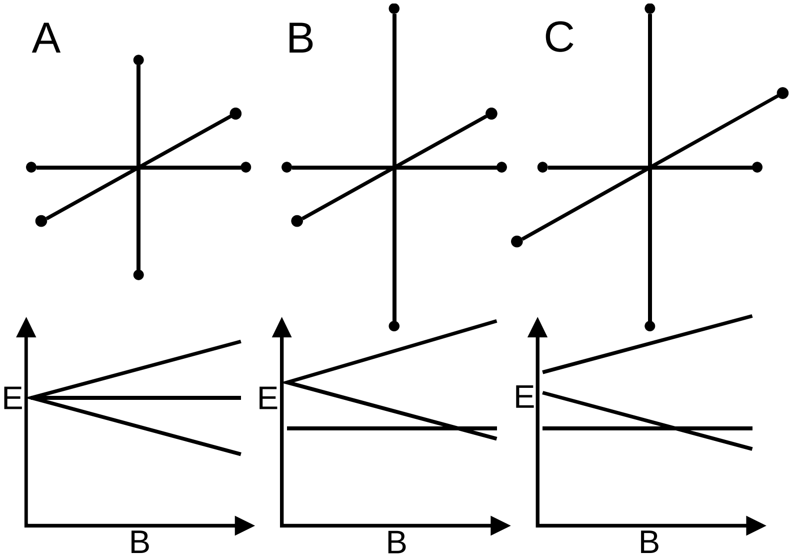

Figure 1.3: Surroundings and energy levels for a triplet ion in an undisturbed (A), axial distorted (B) and rhombically distorted (C) octahedral crystal field

degeneracy between the X- and Y-axis (eq: 1.6). It is common practice to report both D and E in cm^{-1}[9].

$$\mathcal{H} = \mu_B \overrightarrow{B}\overline{\overline{g}}\overrightarrow{S} + D\left(S_z^2 - \frac{S\,(S+1)}{3}\right) + E\left(S_x^2 - S_y^2\right) \tag{1.6}$$

1.2 Benefits of high(er) frequencies

Recording EPR spectra at high frequencies (f > 100 GHz) has a number of advantages over the traditional EPR frequencies of 9, 22 and 35 GHz, such as increased g-tensor resolution, the ability to measure spin systems with a large zero field splitting, the possibility of broad band / multi-frequency measurements and (theoretically) an increase in the overall sensitivity.

1.2.1 Increased g-tensor resolution

The effective g-value is the ratio between frequency and magnetic field. Near identical values for g in an anisotropic spin system leads to broadened

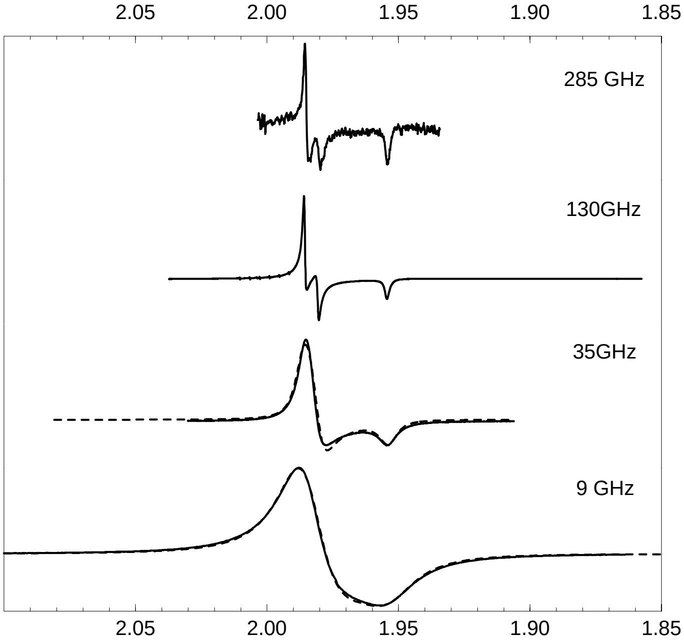

Figure 1.4: The influence of increasing frequency on the resolution of the g-tensor for the anisotropic spin system Na_3CrO_8. The horizontal axis is expressed in the g-factor value. (Reproduced from [10]).

resonances with little or no structural features, see figure 1.2. Increasing the frequency directly increases the difference in resonant magnetic field (eq. 1.7):

$$\Delta B_{g1,g2} = \frac{\hbar\omega}{\mu_B \Delta S_z}\left(\frac{g_2 - g_1}{g_1 \cdot g_2}\right) \tag{1.7}$$

The influence of increasing g-tensor resolution can be quite dramatic as can be seen in the spectra of Na_3CrO_8 (fig. 1.4).

1.2.2 Large zero field splittings

In spin systems with more than 1 unpaired electron, only transition between energy levels that are 1 quantum number (m) apart are allowed ($-\frac{1}{2}$to $\frac{1}{2}$, 0 to 1 . . .). The centers of the energy levels ([$-\frac{1}{2}$, $\frac{1}{2}$], [$-\frac{3}{2}$, $\frac{3}{2}$] . . .) are separated by the zero field splitting. The larger energy quantum allows direct measurement of the Δm = 1 transitions in integer spin systems, resulting in a more accurate determination of the zero field splitting and the g-values (fig. 1.5). At lower frequencies these systems can only be studied through mixing of the electronic states when the molecular and magnetic axis are not lined up ($\theta \neq 0$). The g-values and the zero field splitting are then assessed from variations in the relative intensity at different magnetic fields and temperatures in a rather indistinct manner.

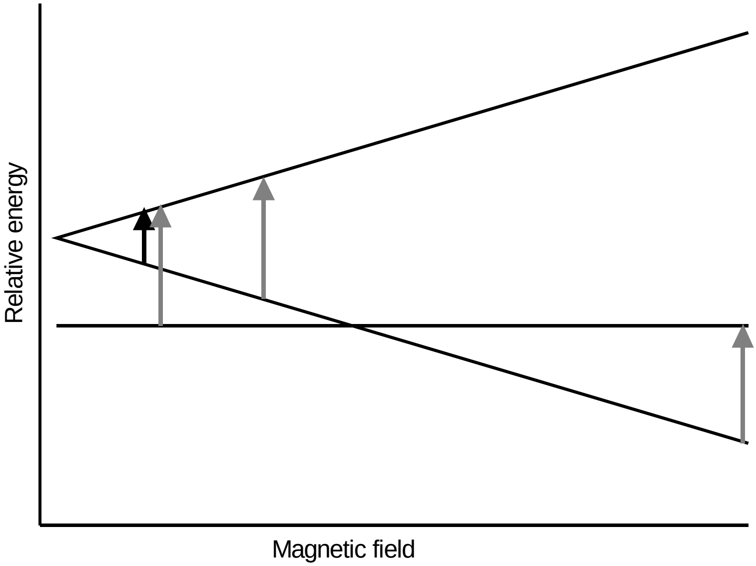

Figure 1.5: Comparison of high- (gray) and low-frequency (black) resonances for an integer spin system ($S = 1$) with a large zero field splitting. The Magnetic field is assumed to be parallel to the zero field splitting axis.

1.2.3 Theoretical increase of sensitivity

The minimum number of detectable spins for a resonant experiment (1.8) is given by Poole [6]:

$$N_{min} \propto \frac{V_s}{Q_u \, \eta \, \omega_0^2 \, (P_w)^{\frac{1}{2}}} \tag{1.8}$$

V$_s$ is the sample volume, Q_u is the quality factor of the unloaded resonator, η is the filling factor, ω_0 is the microwave frequency and P$_w$ is the total microwave power. Depending on the external conditions (constant microwave power, constant energy density at the sample or constant energy density in the waveguides) the increase in frequency corresponds to an absolute sensitivity increase with $\omega_0^{\frac{7}{2}}$ to $\omega_0^{\frac{9}{2}}$ assuming constant sample volume while the concentration sensitivity increases with $\omega_0^{\frac{1}{2}}$ to $\omega_0^{\frac{3}{2}}$ for a constant filling factor. [6, chapter 14]. For small increases in frequency at relatively low frequencies (such as going from 22 to 35 GHz) these predictions are relatively accurate. At high frequencies other factors also need to be taken into account, as will be shown in chapter 2.

1.3 Conclusion

In this thesis the building and use of the Nijmegen High Field, High Frequency, broad band operation EPR set-up is described. Focus of this thesis is the study of paramagnetic systems at both sides of a phase transition.

All spin systems in this thesis had been studied before, but due to the combined features of our set-up we have been able to observe *new* phenomena in the detailed pictures obtained from both sides of a phase transition.

Our use of this non-invasive technique that yields information on single spins (as opposed to magnetization experiments) works not only well for crystallographic and collective magnetic phase transitions, but even a phase transition of the paramagnetic spin system itself, from one spin state to another, has been identified.

Bibliography

[1] E. Zavoisky. Paramagnetic relaxation of liquid solutions for perpendicular fields. *J Phys USSR*, IX:211–216, 1945.

[2] P.J.M. van Kan, E. van der Horst, E.J. Reijerse, P.J.M. van Bentum, and W.R. Hagen. Multifrequency EPR spectroscopy of myoglobin. Spectral effects for high spin iron(III) ion at high magnetic fields. *J. Chem. Soc. Far. Trans.*, 94:2975–2978, 1998.

[3] A. Bencini and D. Gatteschi. *EPR of exchange coupled systems.* Springer-Verlag, 1990.

[4] P.W. Atkins. *Physical Chemistry.* Oxford University Press, 1990.

[5] J.W. Orton. *Electron Paramagnetic Resonance, an introduction to transition group ions in crystals.* London Ilife Books LTD, 1968.

[6] C.P. Poole. *Electron Spin Resonance, a comprehensive treatise on experimental techniques.* John Wiley & sons, 1967.

[7] J.R. Pilbrow. *Transition ion electron paramagnetic resonance.* Oxford science publications, 1990.

[8] A. Abragam and B. Bleaney. *Electron Paramagnetic Resonance of Transition Ions.* Clarendon Press, Oxford, 1970.

[9] T.H. Lowry and K. Scheuller Richardson. *Mechanism and theory in organic chemistry, third edition.* HarperCollins, 1987.

[10] A.H. Priem. *Explorations in high-frequency EPR.* PhD thesis, University of Nijmegen, 2002.

Chapter 2

High Frequency EPR techniques

EPR spectroscopy has been limited to the relatively low frequencies developed during radar research for a long time. During, and after, the second world war research was directed towards the development of strong microwave oscillators and sensitive detectors to improve the newly discovered radar systems. Since a few years oscillators for higher frequencies have become commercially available and consequently a number of research groups have started to develop their own high frequency EPR set-ups. Each group has its own particular solutions to the new problems arising because of the higher frequencies and the shorter wavelengths, although recently a form of consensus is beginning to appear. These problems are transmission line losses, design of an equivalent for the microwave circulator and the design of the resonator/sampleholder.

2.1 Transmission lines

The most basic spectrometer consists solely of a source of microwave radiation, a sample located in an external magnetic field and a detector [1], with more or less free radiation propagation in oversized waveguides. This technique is used in combination with far infra-red lasers, in high magnetic field facilities, like Nijmegen (The Netherlands), Tallahassee (Florida, USA), Grenoble (France) and Tsukuba (Japan).

In conventional EPR spectrometers the transmission line consists of single mode waveguides. For frequencies up to about 150 GHz these work satisfactory, but at higher frequencies the small dimensions of the waveguide and in particular the attenuation (α_r given by equation 2.1) becomes problematic. The ohmic losses at high frequencies can amount to a few dB per meter due to the reduced skin depth and hence the increased skin effect resistance, equation 2.2 [2, p. 102].

$$\alpha_r = \frac{8.686 \cdot R_s}{b\left(\frac{\mu}{\varepsilon}\right)^{\frac{1}{2}}\left[1-\left(\frac{\omega_c}{\omega}\right)^2\right]}\left[1+\frac{2\cdot b}{a}\left(\frac{\omega_c}{\omega}\right)^2\right] \tag{2.1}$$

with:

$$R_s = \frac{1}{\sigma\delta} \text{ and } \delta = \left(\frac{2}{\omega\mu\sigma}\right)^{\frac{1}{2}} \tag{2.2}$$

In these equations $\omega_{(c)}$ is the (cut-off) frequency, μ the magnetic permeability, σ the conductivity of the material used and a and b are the dimensions of the cross sections of the waveguide. For the simple TE$_{m0}$ mode α_r in dB per meter is given by equation 2.1.

To minimize the ohmic losses in high frequency EPR oversized circular waveguides and corrugated waveguides can be used. In corrugated waveguides the inside is fitted with ridges with a height of $\frac{\lambda}{4}$ and a spacing sufficient to allow more than 3 ridges per wavelength. Together with using Gaussian feedhorns a rectangular single mode TE$_{01}$ is converted in a combination of a TE$_{11}$ and a TM$_{11}$ circular mode, resulting in the HE$_{11}$ mode (fig. 2.1). The advantage of the "mode conversion" is that the resulting HE$_{11}$ mode has little or no interaction with the walls of the waveguide, thereby reducing the losses considerably [3, 4, 5, 6, 7]

Oversized circular waveguides do not have a HE$_{11}$ mode and the losses are higher compared to corrugated waveguides. However the physical dimensions of the waveguide with respect to the wavelength minimize the interaction with the walls of the waveguide, reducing the losses to an acceptable extend. For a more theoretical approach see reference [8].

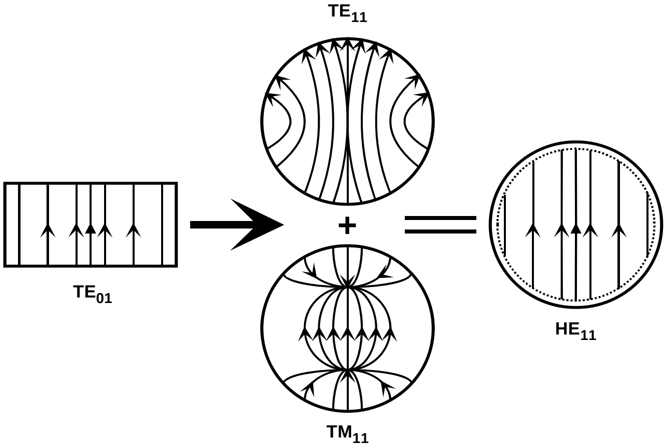

Figure 2.1: The original rectangular TE$_{01}$ mode is converted in both the circular TE$_{11}$ and TM$_{11}$ modes by a Gaussian feedhorn. The two modes combine into the relatively lossless HE$_{11}$ mode in cylindrical corrugated waveguides.

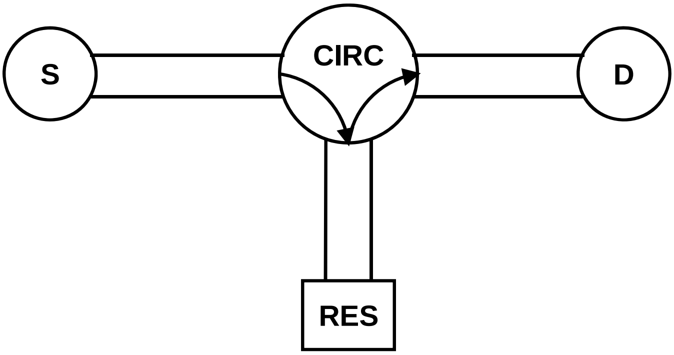

Figure 2.2: Use of directional couplers and circulators in traditional instruments (S is the source, D the detector, RES the resonator and CIRC is the circulator).

2.2 Circulators and directional couplers

Traditional EPR spectrometers use circulators and directional couplers to direct the microwave energy from the source to the sample and back to the detector in reflection-type measurements (fig. 2.2) [2, 9, 10]. This coupler employs the phase coherence of incident and reflected waves. For high frequencies (f $>$ 100 GHz) these devices are not readily available and other solutions were sought. The usual solution for both oversized and corrugated waveguides is a beam splitter with ideally 50 % reflectivity mounted at a 45° angle (fig. 2.3). Reflection setups at higher frequencies become possible this way, but at most 25 % of the output power of the source reaches the detector. To facilitate detection one arm of the beam splitter has a tunable mirror. Off resonance this is tuned such that the observed power on the detector is as low as possible. The absorbance of microwave energy at resonance is then detected using a heterodyne detection scheme.

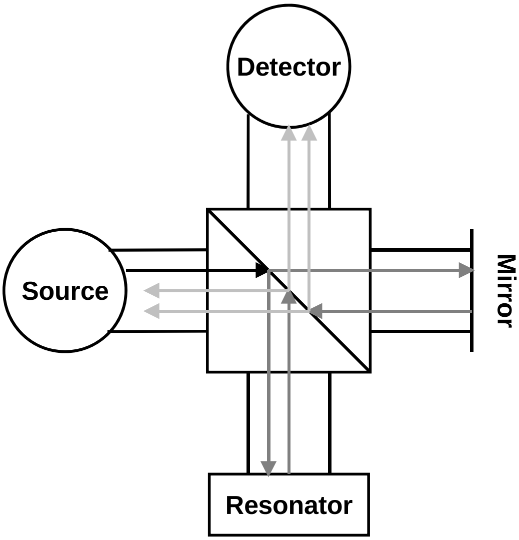

Figure 2.3: Use of beamsplitters and mirrors in our HF set-up. Relative intensities are color-coded. The darker the color, the more intense the beam.

An innovative design for a directional coupler and/or circulator was devised by Smith and coworkers [3, 5, 6]. Using Gaussian beam optics in combination with polarizers and a Faraday rotator (usually a magnetized thin plate of hexaferrite that rotates the incident beam through 45°) an effective circulator was build. The benefit of this type of circulators is that two detection types are supported (see fig. 2.4).

In the first type of experiment the beam coming from the source is polarized in one direction by the polarizer and rotated through 45 degrees by the Faraday rotator before reaching the resonator. In the reverse route the signal coming from the resonator is rotated through 45 degrees by the faraday rotator before being diverted by the polarizer to the detector. This set-up allows the full power of the source to reach the detector.

A different type of experiment is the detection of the cross polarized EPR spectrum. After passing a polarizer the polarized microwave beam interacts with the resonant electron spins in the resonator. Absorption of a left (or right) polarized microwave photon will lead to reflected radiation at an orthogonal (linear) polarization, which can be detected on a near zero

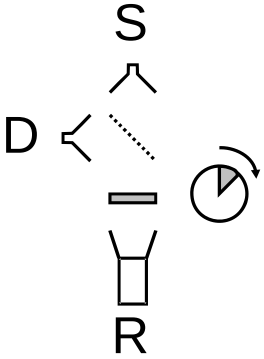

Figure 2.4: Position of the source (S), detector (D), polarizer (P), sample holder / resonator (R) and optional 45° Faraday rotator (gray) for "normal" and "cross polarized" experiments respective of the presence of the Faraday rotator

background. The drawback of these systems is the difficulty to manufacture polarizers of sufficient quality to have a sufficiently effective circulator. Furthermore a phase matching needs to be applied to the Faraday rotators to minimize the reflections for a specific frequency, limiting broad band operation. A last point of concern is the high quality of waveguides needed since even small imperfections can lead to a degradation of the polarization coherence.

2.3 Resonators

A very important part of EPR spectrometers is the microwave cavity or resonator, which acts as a "concentrator" of microwave radiation on the sample. Typically a single standing wave pattern is created within a small space (of the order of the wavelength) with the sample located at maximum microwave magnetic field density. The efficiency of a resonator is expressed in the *Quality* factor or Q, which for an unloaded resonator is the ratio between the stored energy and the energy dissipated per cycle, of the microwave magnetic field (H_m). Losses arise from the dissipation of the surface current density due to the skin effect resistance. If only ohmic losses are taken into account the unloaded Q_u is given by [2]:

$$Q_u = \frac{\omega\mu}{R_s}\frac{\int |H_m|^2 d\tau}{\int |H_{tm}|^2 d\tau} \tag{2.3}$$

In which ω is the microwave frequency, μ the magnetic susceptibility, R_S the skin effect resistance, H_m the magnetic field at the part of the cycle denoted by m and H_{tm} the maximum tangential field. Q increases with increasing frequency, resulting in an increase of the sensitivity (equation 1.8). However, with increasing frequency the wavelength decreases and for a single mode resonator the dimensions of the resonator are scaled down proportional to the frequency. For high frequencies (f > 100 GHz) the resonator becomes very small and the dielectric losses (ϵ) of the sample increase, resulting in an overall decrease of the quality factor of the loaded resonator Q_l:

$$\frac{1}{Q_l} = \frac{1}{Q_u} + \frac{1}{Q_\epsilon} \tag{2.4}$$

Therefore a number of resonators have been developed in recent years. The most widely used will be discussed below.

2.3.1 Single mode resonators

The most commonly used resonators are the single mode rectangular and cylindrical resonant cavity. Both types of resonators support both TE_{mnp} and TM_{mnp} modes, depending on the exact geometry and coupling. For the rectangular resonator the subscripts m, n and p denote the number of half wavelengths in the x, y and z-directions. In cylindrical resonators the subscripts refer to the number of half cycle variations in the angular (ϕ), radial (r) and longitudinal (z) directions.

By scaling the cavity dimensions a,b and d of the rectangular resonator to the wavelength in the x-, y- and z-directions, the resonance frequency $2\pi \mathrm{f}_0$ is given by [2]:

$$\omega_0 \left(\mu\epsilon\right)^{\frac{1}{2}} = \pi \left(\frac{m^2}{a^2} + \frac{n^2}{b^2} + \frac{p^2}{d^2}\right)^{\frac{1}{2}} \tag{2.5}$$

For the TE_{102} mode the dimensions are λ and 2λ respectively, therefore if the frequency increases the resonator dimensions should decrease accordingly. The overall quality factor for both type of resonator is linked to their size. To operate at 9 GHz the dimensions of the single mode resonator are 16.7 x 8.3 x 33.3 millimeters. The same resonator constructed for 285 GHz would have dimensions of 0.53 x 0.26 x 1.05 millimeters. The effect of proportionally scaled dimensions on the quality factor, and thereby on the minimum number of detectable spins (eq. 1.8) is negligible[1]. The same sample size now has a larger filling factor (η) Increasing the sensitivity. However the increase in relative sample size also increases the dielectric losses reducing the overall quality factor (eq. 2.4), the net effect depends on the individual conditions for each sample. Furthermore, depending on the sample size with respect to the resonator size, a shift in resonance frequency can also be observed since the wavelength in the sample will be longer than in free air. In extreme cases the frequency shift will be sufficient to make

---

[1] For the precise calculations and the necessary equations the reader is referred to reference [2].

the loaded resonator incompatible with the source and / or the optimal frequency of the transmission lines.

2.3.2 Whispering gallery resonators

A special type of resonator for high frequency EPR is the whispering gallery mode (WGM) resonator, consisting of a dielectric disc placed perpendicular to the external magnetic field. A standing wave is induced at the rim through the evanescent field of a quartz waveguide placed close to the rim of the disc (fig. 2.5). The precise coupling is tuned by the proximity of a metal ring parallel to the disc [11, 12].

For this type of resonator the sample can be mounted in different ways. The first method is to place the sample on the edge of the disc in a "belt type" loop, which ensures a high filling factor, but is only suitable for powdered samples. In the second method the sample is located between two discs in a "sandwich" construction, which is suitable for small volumes of liquid or powdered crystals. Both type of WGM resonator have a filling factor near unity and high Q-factor (10000 and upwards) making the WGM resonator very sensitive. In the stacked configuration only a relatively small part of the sample, placed close to the outer rim, interacts with the microwave radiation. Therefore the sample not contributing to the EPR resonance, also does not contribute to the dielectric losses. The

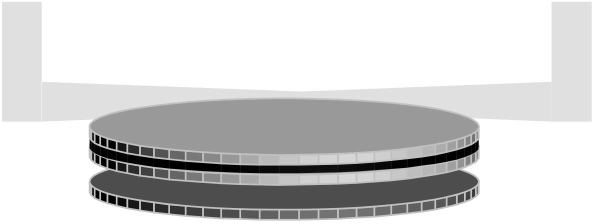

Figure 2.5: A WGM-resonator, shown here in the stacked configuration. The (black) sample, sandwiched between two discs made of polyethylene or quartz, is placed before a quartz waveguide. The metallic ring used to optimize the tuning can be seen underneath.

drawback of WGM resonators at conventional frequencies is the relatively large space needed, limiting the usefulness to large bore magnets, while for high magnetic fields small bores are preferred.

2.3.3 Fabry-Perot resonators

The cylindrical Fabry-Perot resonator (see fig. 2.6) employs a standing wave pattern between two mirrors, with the coupling hole in one of them. In most cases the bottom mirror is concave to reduce radiation losses and increase mode stability. Instead of a coupling hole as in traditional spectrometers, also coupling through a fine wire mesh between the waveguide and the resonator is a viable option. In this case the surface of the mesh acts as a mirror [3, 5, 6, 7, 13, 14]. The size of the sample volume is comparable to an oversized resonator, but in a Fabry-Perot resonator the mode pattern is known and consists of a number (n) of half cycle variations in the z-direction and none (or 1) half cycles in the x- and y-directions.

Due to the 1-dimensional nature it is one of the few resonators that can be tuned while in operation, enabling multi frequency operation. The range

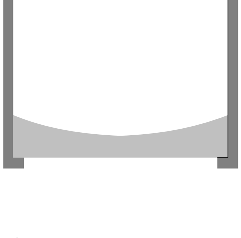

Figure 2.6: Tunable Fabry-Perot resonator as used in the Nijmegen HF-EPR set-up. The top mirror is connected to the waveguide and the bottom mirror is connected to the external sidewalls and can be tuned from outside the cryostat.

of operation is dependent on the curvature and the displacement range of the bottom mirror. Tunability of the resonator is a benefit when the tunability of the source is limited. A ”drawback” of Fabry-Perot resonators is the limited volume of sample that can be applied. The known intensity optimum for microwave radiation, is located parallel and close to the bottom mirror and is insensitive to tuning. The small sample size is compensated by the relatively high Q factors (> 5000) that can be obtained, resulting in a better sensitivity than oversized resonators, but at the cost of a more stringent tuning procedure.

2.3.4 Oversized resonators

Oversized resonators are a scaled up version of single mode resonators, but without a well defined standing wave pattern. For instance the resonator designed by Boonman [8] for the Nijmegen HF-EPR set-up is a 12 mm i.d. cylinder with a length of 25 mm and an axial coupling hole. In the range between 30 and 190 GHz with a tunable source a resonance can always be found near the desired experimental frequency. Q-values of the oversized resonators are about the same order of magnitude (1000 - 5000) as single mode resonators. The major advantages are the ability to measure at a broad range of frequencies without changing the set-up and the availability of a high Q resonator with fairly large sample sizes.

Normally the standing wave pattern in these resonators is not known, but by insulating the endcap no current can pass from the cavity walls to the endplate [8]. This results in wave patterns resembling a TE_{0mp} mode with the maximum microwave magnetic field densities parallel and close to the end plate. Powders can be spread uniformly over the endcap, while single crystals are better placed slightly of center since in even modes a node of microwave intensity will be located there.

2.3.5 Non resonant sample holders

Non resonant sample holders are constructed from a small piece of waveguide with a reflector at the terminus. Although technically not a resonator, they can be used to good effect in reflective EPR experiments. The sensitivity of these sample holders is better than one would expect considering their very low Q-factor. Since there is no dominant mode, no account has to be taken of the position of maximum microwave density and relatively large amounts of sample can be used. The major advantages are the wide ranges of frequencies and samples that can be covered. The resonance condition only has a lower limit determined by the maximum wavelength that would fit inside the sample holder. The closed structure and relative size are well suited to contain single crystals, powders, frozen solutions and solidified gases.

2.4 The Nijmegen HF-EPR set-up

For the Nijmegen HF-EPR set-up some of the sensitivity was sacrificed in favor of multi-frequency operation, especially concerning the resonator. HF-EPR on a number of frequencies with large differences yields more accurate information than experiments performed using a small frequency range around a single (high) frequency.

2.4.1 Source and detection

The set-up uses a commercial Microwave Vector Network Analyzer (MVNA), from *ABmm*, Paris. The MVNA is a solid state based vector network analyzer capable of measuring the amplitude and phase (absorption and dispersion) of a tunable frequency signal. Non-linear devices are used for frequency multiplication and harmonic mixing to perform down-conversion and enable heterodyne detection [15]. A basic diagram of operation is drawn in figure 2.7. The harmonic millimeter wave frequencies F_{MM} are generated by the harmonic generator (HG) powered by the tunable source 1 at frequency F_1:

$$F_{MM} = \sum_{1}^{N} A_N N F_1 \tag{2.6}$$

with A_N the efficiency of the microwave generator at a specified harmonic (N), determined by the mechanical tuning of the harmonic generators. The harmonic mixer (HM) powered by source 2 at a frequency F_2 down converts the high frequency signal F_{MM} to a low frequency (Megaherz range) signal F_{IF} defined by:

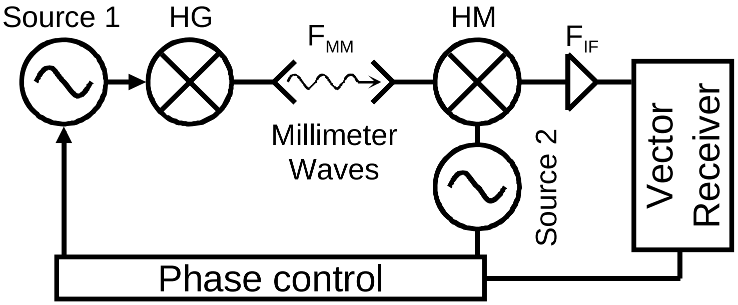

Figure 2.7: Schematic MVNA set-up configured for low frequency operation.

$$F_{IF} = \sum_{1}^{M} \sum_{1}^{N} ((A_N N F_1) - (A_M M F_2)) \tag{2.7}$$

The efficiency of the two harmonic generators is optimized for the desired operational frequency. The frequency difference between F_1 and F_2 is chosen so that the interference frequency at the same higher harmonic of the base frequency at the desired operational frequency matches the frequency of a narrow bandwidth filter before down-conversion.

Phase locking the two sources allows the detection of the phase and amplitude information at the operational frequency. Before detection the signal is down-converted to 488 Hz and fed into a lock-in amplifier.

At operating frequencies of 190 GHz and higher a grating monochromator is placed between the source and the rest of the set-up in order to minimize the background on the detector. The source was coupled to a monochromator by a feedhorn, while at the exit a concave mirror is used to focus the microwave radiation in the waveguide. The walls of the waveguide have been tapered to minimize reflections due to impedance mismatch.

Using multiple harmonic mixers and generators, continuously tunable frequency coverage between 30 and 190 GHz is achieved with the Schottky diodes operating at a base frequency between 8 and 18 GHz. For frequencies of 190 GHz and higher an additional Gunn oscillator is used operating at

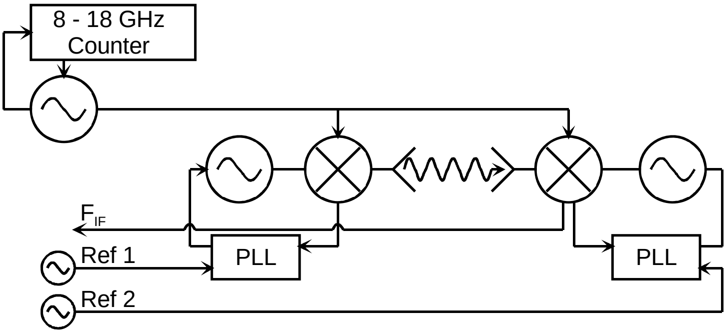

Figure 2.8: Schematics for MVNA operation for frequencies of 285 GHz and higher. Both PLL controlled Gunn diodes and their reference arms are included.

95 GHz. At 285 GHz and higher a second Gunn oscillator is used at the detection side. Both harmonic mixers following the 95 GHz Gunn oscillators are coupled to mechanically tunable cavities to enhance the intensity of the desired frequency with respect to the other frequencies. A schematic diagram of high frequency operation (fig. 2.8) shows both PLL controlled Gunn oscillators with the additional references.

2.4.2 Transmission lines

To minimize ohmic losses, and maintain wide frequency coverage we used cylindrical waveguides with an inner diameter of 13 millimeter. Smooth waveguides were preferred above corrugated waveguides because:

1. Corrugated waveguides are designed for a specific small frequency range. Smooth waveguides on the other hand offer operation for frequencies from 60 GHz upwards for the tapered 13mm inner diameter waveguides.

2. Smooth waveguides are easier to maintain. Corrugated waveguides are more susceptible to dirt (larger surface area) and small imperfections can destroy the HE_{11} mode. Furthermore due to the ridged structure they are more difficult to clean than smooth waveguides.

The last 10 centimeters before the resonator / sample holder were tapered to an inner diameter of 2.5 millimeter to focus the microwave energy to the resonator. A beam splitter was used as circulator (fig. 2.3) with various mylar and PE (Poly-Ethylene) sheets as reflector, ranging in thickness from 100 to 250 μm depending on the frequency. The reflection of the reference arm is matched in intensity, but at a 180° phase shift to the off resonance signal of the resonator. The low microwave intensity allows the detector to be run at higher sensitivity.

2.4.3 Available resonators

Fabry-Perot resonator

The tunable Fabry-Perot resonator, made in house, is the most sensitive resonator available for the HF-EPR set-up (fig. 2.6). Using a MgO sample with a 0.003% Mn^{2+} impurity sensitivities in the order of 10^{10} spins per gauss could be obtained at 190 GHz.

For comparison the minimum number of detectable spins using non-resonant sample holders was estimated to be in the order of 10^{12} to 10^{13} spins per gauss, for the $S = \frac{5}{2}$ signal.

Oversized sample holder

The oversized sample holder described in section 2.3.4 was used for frequencies from 30 GHz up to and including 190 GHz. Single crystals, powdered samples and frozen solutions have been measured usually with sufficient sensitivity and range of operation. At these frequencies it is more sensitive than the non-resonant sample holders due to it's high Q-factor. At higher frequencies (285 GHz and up) the size of the resonator was such that no specific resonance frequency for the resonator could be detected, causing it to behave as a non-resonant sample holder.

Non-resonant sample holders

The work horses are the non-resonant sample holders, because of their flexibility in both frequency and sample handling capabilities. Two types of non-resonant sample holder have been constructed. The first consisted of a piece of quartz capillary with a small mirror at the bottom. The outside was wrapped in aluminum foil to prevent excessive loss of microwave radiation. To prevent contact with air PE endcaps, coated in apiezon N, were used. A nylon jacket was fitted to protect the fragile capillary. The second sample holder was constructed out of a small cylinder of stainless steel (5 mm i.d. x 20 mm) allowing operation upwards of 60 GHz. A nylon disc could be fitted in the threaded top to prevent contact with air. In the oxygen experiments this disc was removed to allow condensation of the gas-mixture in the sample holder. One stainless steel cylinder was fitted with a modulation coil for field derivative measurements.

2.4.4 Available cryostats

Two types of cryostat are available at the Nijmegen set-up. The first is a traditional bath-cryostat which is filled with liquid helium. Heat transfer between the waveguide and the surrounding liquid helium dewar is trough a small amount of He exchange gas. A small heater and a thermometer in close proximity to the sample holder / resonator allow a small temperature range to be achieved. The benefit of this set-up is that it is easier to operate at low temperatures, but the slow decrease of the helium level by evaporation influences the length of the transmission lines going down the magnet. Depending on a combination of microwave frequency and scan time this can lead to a constant drift in the relative phase (and amplitude) of the background upon which the EPR signal is superimposed.

The flow cryostat which we used does not exhibit this problem as extensively. A heater and a capacitive[2] thermometer coupled to a PID controller allow a temperature from 4 to 300 K with an accuracy of ± 0.25 K to be maintained over long periods (multiple hours). The major drawback of this type of cryostat is that, with the long transmission line up and down the magnet (up to one meter), it takes a few hours before the temperature gradient over the transmission line is sufficiently stable to measure a near driftless EPR signal.

2.4.5 Data analysis

In using the MVNA, a set of data is obtained for every magnetic field sweep which contains a complex resonant and a complex non-resonant part, the leak vector: A_M(B,T)exp(iϕ_M(B,T)) and $A_L$exp(iϕL) respectively. By plotting the phase and amplitude, the complex leak vector can be determined by comparing the position of the resonance in the complex plane, with the ideal resonance passing through the origin of the complex plane. Assuming the leak vector is constant over the whole measurement it can be subtracted from the measured signal. The complex normalization factor $A_N$exp(iϕN) obtained from the same fitting procedure rotates the structure in the polar plane to the position of an ideal resonance. The remaining signal can now be converted into a complex signal corrected for instrumental effects (eq. 2.8) as visualized in figure 2.9.

$$A(B,T)\,exp(i\phi(B,T)) = \frac{A_M\,(B,T)exp(i\phi_M(B,T)) - A_L\,exp(i\phi_L)}{A_N\,exp(i\phi_N)} \tag{2.8}$$

where the amplitude A(B,T) and phase ϕ(B,T) signals correspond to the absorption and dispersion respectively[3] Fig. 2.9 shows the procedure used throughout this thesis to obtain absorption and dispersion plots versus

---

[2] A capacitive thermometer is not sensitive to the magnetic field.

[3] The (abbreviated) method of leak vector subtraction has been devised by M.E.J. Boonman. For a full discussion the reader is referred to reference [8].

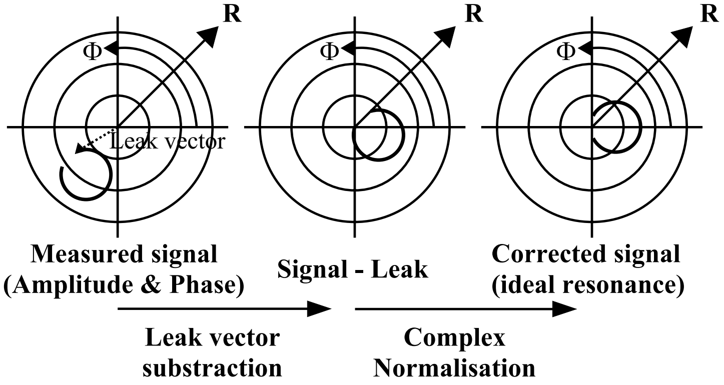

Figure 2.9: Graphic representation of the leak factor subtraction process devised by Boonman [8].

magnetic fields, without leak factors. The transformed experimental plots are then compared to simulations based on the relevant spin Hamiltonian, in which the g-values, D, E and occasionally the spin state are varied manually until good agreement between experiment and calculation is obtained. Preferably the same parameter set should yield good results at multiple temperatures and/or frequencies. Positions of maxima are based on the eigenvalues, the normalized relative intensities are based on the transition probability combined with a Gaussian lineshape function [1]:

$$P_{\alpha\to\beta} = \frac{2\pi}{\hbar} \langle \beta \mid H\Psi \mid \alpha \rangle^2 \frac{1}{\sigma_G\sqrt{2\pi}} e^{-\frac{1}{2}\left(\frac{\omega-\omega_0}{\sigma_G}\right)^2} \tag{2.9}$$

where σ_G is the half peak-peak width of the first derivative and taking into account the Boltzman distribution:

$$P = \frac{e^{\frac{\Delta E_{(n-1)-n}}{kT}}}{\sum_n e^{\frac{E_n}{kT}}} \tag{2.10}$$

2.5 Conclusion

As has become clear from the previous sections there is no golden rule to building a HF-EPR set-up. In building the Nijmegen set-up the overall design has been optimized for flexibility and broad band operation although a number of components still have been maintained for a more increased sensitivity.

The flow cryostat had been a practical choice because it allows a more stable operation at low temperatures then a bath cryostat. This is especially so for the broad band sweeps of over the magnetic field range of several tesla that lasted up to an hour.

To prevent a heating and venting cycle of the cryostat when a new frequency range was chosen the sample holders were preferably non-resonant. This allowed operation at most frequencies. The same reasoning was used in preferring smooth waveguides instead of corrugated waveguides. The former also have the benefit of being easier to clean. Both choices have been a trade-off for flexibility from sensitivity. If a more sensitive set-up is needed use can be made of either a single mode resonator (up to 190 GHz) or a Fabry-Perot resonator, which are also present.

Bibliography

[1] J.R. Pilbrow. *Transition ion electron paramagnetic resonance.* Oxford science publications, 1990.

[2] C.P. Poole. *Electron Spin Resonance, a comprehensive treatise on experimental techniques.* John Wiley & sons, 1967.

[3] G.M. Smith. Millimeter waves and gaussian beams. Lecture serie at the University of Nijmegen, 1997.

[4] G.M. Smith, C.P. Unsworth, S. Kang, D. Franklin, and J.C.G. Lesurf. Design and applications of high frequency quasi optical faraday rotators. *21*$^{\mathrm{ST}}$ *int. conf. infrared &* MM *waves, Berlin*, page Bth4, 1996.

[5] G.M. Smith, J.C.G. Lesurf, R.H. Mitchell, and P.C. Reide. A MM-wave quasi-optical electron spin resonance spectrometer. *Res. Sci. Int.*, 69:3924–3937, 1998.

[6] G.M. Smith and J.C.G. Lesurf. A highly sensitive millimeter wave quasi-optical FM noise measurement system. *IEEE Trans. MTT.*, 39:2229–2236, 1991.

[7] T. Matsui, K. Araki, and M. Kiyokawa. Gaussian beam open resonator with highly reflective circular coupling regions. *IEEE Trans. MTT.*, 41:1710–1713, 1993.

[8] M.E.J. Boonman. *Millimeter wave spectroscopy in high magnetic fields.* PhD thesis, University of Nijmegen, 1999.

[9] J.W. Orton. *Electron Paramagnetic Resonance, an introduction to transition group ions in crystals.* London Ilife Books LTD, 1968.

[10] A. Abragam and B. Bleaney. *Electron Paramagnetic Resonance of Transition Ions.* Clarendon Press, Oxford, 1970.

[11] G. Annino, M. Casettari, I. Longo, M. Martinelli, P.J.M. van Bentum, and E. van der Horst. A novel probe head for high-field, high-frequency electron paramagnetic resonance. *Rev. Sci. Instrum.*, 70:1787–1793, 1999.

[12] G. Annino, M. Cassettari, and M. Martinelli. Analysis of 'stacked' whispering gallery dielectric resonator for submillimeter ESR spectroscopy. *Chem. Phys. Lett.*, 281:306–311, 1997.

[13] R. Ulrich. Far-infrared properties of metallic mesh and its complementary structure. *Infra. Phys.*, 7:37–55, 1967.

[14] P.A.R. Ade, A.E. Costley, C.T. Cunningham, C.L. Mok, G.F. Neill, and T.J. Parker. Free standing grids wound from 5 μm diameter wire for spectroscopy at far infrared wavelengths. *Infra. Phys.*, 19:599–601, 1979.

[15] French patent from September 1989, Centre National de La Recherche Scientifique-Ecole Normale Superieure; U.S. patent, P. Goy and M. Gross, no: 5,119,035 2nd of June 1992; also patented in Europe and Japan.

Chapter 3

The ground state of Ni^{2+} doped in $Zn(en)_3(NO_3)_2$

Abstract

EPR measurements of $Zn(en)_3(NO_3)_2$ doped with Ni^{2+} ions are characterized by the $S = 1$ triplet spectrum of the Ni^{2+} ions. In the center of the $S = 1$ multiplet a strong additional signal, not originating from the $S = 1$ multiplet, is observed. Previously this additional signal was attributed to a double quantum resonance of the Ni^{2+} ion.

The observed $S = 1$ resonances of the Ni^{2+} ions are in good agreement with simulations based on the fixed set of g-values: $g_{\|} = 2.160$ and $g_{\perp} = 2.148$ for both crystallographic phases of $Zn(en)_3(NO_3)_2$. Passing through the crystallographic phase transition temperature the zero field splitting of the triplet decreases from $+0.83\ \text{cm}^{-1}$ to $+0.77\ \text{cm}^{-1}$. Simultaneously a rhombic distortion with a narrow distribution around $0.10\ \text{cm}^{-1}$ appears.

Below the transition temperature the additional signal shows structural features incompatible with double quantum resonance theory, but can be explained by an unresolved $S = \frac{3}{2}$ spin state. Therefore it is proposed that the resonance previously attributed to a double quantum resonance originates from an $S = \frac{3}{2}$ paramagnetic center in the crystal, most likely Ni^{3+} ions in a cubic ligand field.

3.1 Introduction

The study of the high field EPR transitions of Ni^{2+} ions at the Zn^{2+} sites in the matrix of Zinc ethylene diamine nitrate ($Zn(en)_3(NO_3)_2$) crystals was motivated by the speculations of Van Dam [1, 2] that in this system an unusually strong double quantum resonance[1] is observed superimposed on the $S = 1$ spectrum, while simultaneously the $S = 1$ resonances remain intense. Normally single quantum resonances become less intense due to saturation induced by the large amount of microwave energy necessary to make the double quantum resonance more prominent [6, 7, 8]

$$2\hbar\omega_{photon} = \Delta E_{m\rightarrow m+2} \tag{3.1}$$

A double quantum resonance is the simultaneous absorption of two quanta resulting in a single transition (see fig. 3.1) as opposed to "normal" EPR transitions in which only a single quantum is absorbed per transition. The double quantum resonance is most intense if the intermediate state is real, i.e. it is an eigenstate of the spin Hamiltonian [6, 9, 10]. For a triplet state with an axial g-tensor and a finite zero field splitting this coincidence occurs at the so-called magic angle orientation ($\theta = 54.7°$) of the crystal axis with respect to the magnetic field orientation.For a random distribution this condition only applies to a small fraction of the sample. It is therefore remarkable that the signal associated with this orientation should be strongly present.

$Ni:Zn(en)_3(NO_3)_2$ is an exceptional matrix for two reasons: first, the double quantum resonance is not only strong enough to be observable under normal EPR conditions. Usually to observe the double quantum resonance the microwave intensity has to be raised so high that the single quantum EPR signals are highly saturated. Secondly the double quantum resonance is sufficiently removed from the single quantum resonances (for resonant magnetic field value) to observe both signals simultaneously. This yields an opportunity to study the effects of a phase transition in the matrix on the double quantum resonance, while simultaneously comparing the observed

---

[1] The term double quantum resonance in this thesis is used exclusively for the process described by equation 3.1 and not the technique of measuring distances as performed by Freed and coworkers [3, 4, 5]

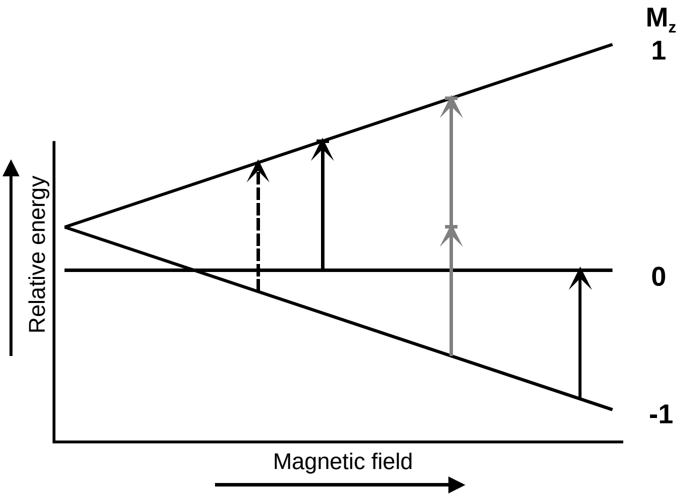

Figure 3.1: Transitions in an $S = 1$ triplet system for $B_0 \parallel S_z$. Solid arrows: main $S = 1$ resonance, dashed arrow: weak half field resonance (single quantum $\Delta m = 2$) and gray arrows: the double quantum resonance ($\Delta m = 1+1$)

parameters with those of the single quantum resonance to determine which observed effects are intrinsic and which are caused by the saturation of the single quantum resonance.

Recently an EPR study of Ni:Zn(en)$_3$(NO$_3$)$_2$ at high temperature and two frequencies demonstrated a double quantum resonance with a linear dependence on the square root of microwave power [1, 2]. Theoretically the dependence on microwave power of this second order process should be proportional to $P^{\frac{3}{2}}$, with P the incident microwave power in mW [9, 10, 11, 12, 13]. This discrepancy was explained by a simultaneous excitation of two single quantum transitions, leading to a greater population difference between the participating energy levels. To understand the behaviour of the double quantum resonance of Ni:Zn(en)$_3$(NO$_3$)$_2$ a high frequency EPR study at both high and low temperatures was performed.

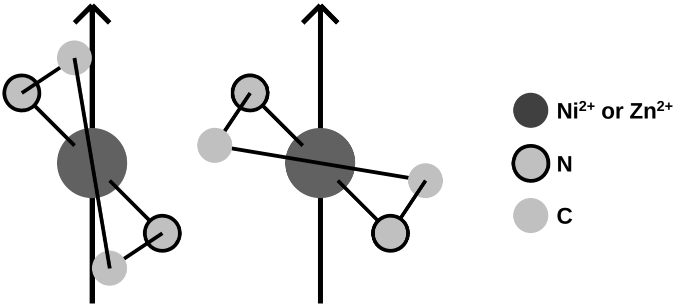

Figure 3.2: The δ-form (left) and the λ-form (right) orientation of the ethylenediamine ligand on the central ion, with respect to the C$_3$ axis of the unit cell (after reference [16]).

3.2 Crystallography of Ni:Zn(en)$_3$(NO$_3$)$_2$

The crystals of Ni:Zn(en)$_3$(NO$_3$)$_2$ were obtained by slow evaporation of Ni(en)$_3$(NO$_3$)$_2$ (*aq*) and Zn(en)$_3$(NO$_3$)$_2$ (*aq*), in accordance with the method published by Prasad *et. al.* [14]. The final concentration of nickel in the crystals used was about 4%. Introduction of nickel in the crystallographic site of zinc is not reported to have a significant influence on the crystal structure, apart from a small increase of the phase transition temperature, from 141 K in pure Zn(en)$_3$(NO$_3$)$_2$ [15] to 146 K with 4% Ni doping [16]. Below the phase transition temperature a reorientation of one of the ethylenediamine groups from the δ-form ($\wedge - \delta\delta\delta$) to the λ-form ($\wedge - \delta\delta\lambda$) (fig. 3.2) introduces a rhombic distortion and decreases the zero field splitting [15, 16].

3.3 Experimental set-up

All measurements were performed on finely powdered crystals loaded in non-resonant sample holders. Temperatures above and below the phase transition temperature of Ni:Zn(en)$_3$(NO$_3$)$_2$ were achieved with the flow cryostat described in section 2.4.4. Spectra were recorded at 190 GHz using a frequency tunable, solid state source operating at the second harmonic of 95 GHz with an output power of about 1 mW and at 130 GHz with a single frequency oscillator with an output power of 10 mW. The field modulated signal for both frequencies was detected by means of an InSb bolometer.

3.4 The S = 1 resonances of Ni:Zn(en)$_3$(NO$_3$)$_2$

In figures 3.3 and 3.4 we show typical results for different frequencies and temperatures. The parameters of the Ni^{2+} centers are determined from a comparison between experiment and simulation using spin Hamiltonian 3.2. The half field, single quantum Δm = 2 transition did not yield additional information, and will not be discussed further. The central resonance (C) in the spectra of figures 3.3 and 3.4 originates from a different spectroscopic process and will be discussed in section 3.5.

$$\mathcal{H} = \mu_B \overrightarrow{B}\overline{\overline{g}}\overrightarrow{S} \; + \; D\left[S_z^2 - \frac{S(S+1)}{3}\right] \; + \; E\left[S_x^2 - S_y^2\right] \tag{3.2}$$

3.4.1 190 K data

The data at 190 K for both frequencies clearly shows the two high field resonances one would expect for a triplet system without a rhombic distortion (fig. 3.3). Previously reported values of g and D for the Ni^{2+} ions inserted in an Zn(en)$_3$(NO$_3$)$_2$ matrix range from an isocratic g_{iso} = 2.200 ± 0.006 to $g_{||}$ = 2.181, $g_{\perp}$ = 2.156 with D = -0.832 cm^{-1} [1, 2, 14, 16].

In the current experiments good agreement between experiment and simulation is achieved using $g_{||} = 2.160$ and $g_{\perp} = 2.148$ with D = +0.83 cm^{-1}.

3.4.2 115 K data

Lowering the temperature to 115 K, below the phase transition temperature of 142 K, introduces a rhombic distortion. The rhombic distortion is apparent from the change in the observed spectra of both frequencies (fig. 3.4). If the zero field splitting is dropped from +0.83 cm^{-1} to +0.77 cm^{-1} and a rhombic distortion of +0.10 cm^{-1} is taken into account good agreement between the current experiments and simulations can be achieved while the g-values need not be adjusted ($g_{||}$ = 2.160 and $g_{\perp}$ = 2.148).

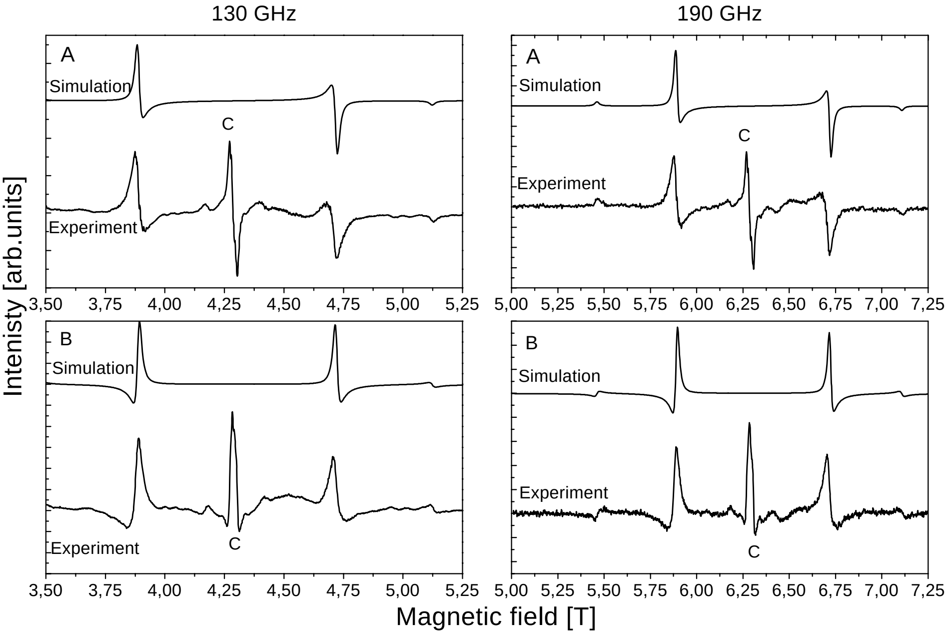

Figure 3.3: The 130 and 190 GHz $S = 1$ resonances of Ni:Zn(en)$_3$(NO$_3$)$_2$ at 190 K. Both the absorption (A) and the dispersion (B) are plotted. All simulations are based on: $g_{||} = 2.160$, $g_{\perp} = 2.148$ and $D = +0.83$ cm^{-1}.

On closer examination it can be seen in figure 3.4 that the observed height of the signals at the extremes of the $S = 1$ multiplet (A) are simulated with an intensity that is slightly too low (simulation plotted below the experimental data).

The rhombic distortion is introduced by flipping one carbon backbone in the crystallographic unit cell (fig. 3.2). A previous study on single crystals by Wilson *et. al.* [16] revealed that there are six sites in the low temperature phase which are all equivalent apart from their orientation.

A small distribution of the orientations of the carbon backbones, or small inequivalencies between the six states can lead to a small distribution in the rhombic distortion. A simulation of the low temperature spectrum at

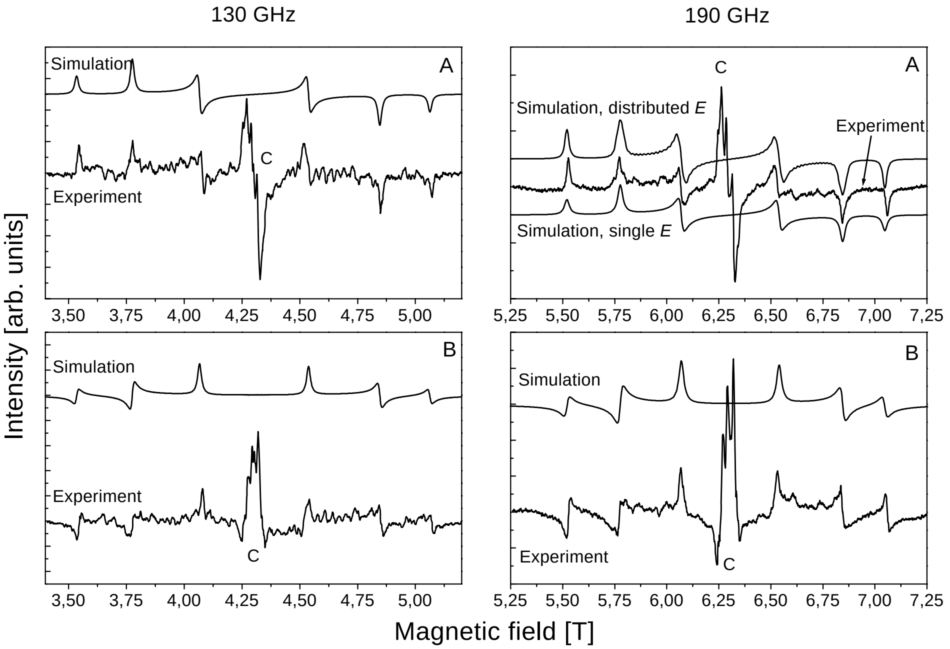

Figure 3.4: The 130 and 190 GHz $S = 1$ resonances of Ni:Zn(en)$_3$(NO$_3$)$_2$ at 115 K. Both the absorption (A) and the dispersion (B) are plotted. All simulations are based on: $g_{\|} = 2.160$, $g_{\perp} = 2.148$, $D = +0.77$ cm^{-1} and $E = +0.1$ cm^{-1}. For the 190 GHz absorption resonance an additional simulation is plotted with a small distribution in the rhombicity ($E = +0.09$, $+0.10$ and $+0.11$ cm^{-1} in relative intensities 1:2:1)

190 K with a minimal distribution ($E = +0.09$, $+0.10$ and $+0.11$ cm^{-1} with relative intensities of 1:2:1) was made. The line shape of the distribution is plotted above the experimental data in figure 3.4. Clearly the relative height of the simulations with respect to the experimental data has improved. The result of the distribution is not so much to increase the height of the outermost signals, but to decrease the observed height of the inner transition as a result of line broadening.

The observed reproducibility of the distribution is such that we believe that this distribution is inherent for this compound. From the current experiments we cannot conclude whether it is the relative orientation of one of the carbon backbones or an inequivalency in the six sites. It is possible that single crystal measurements on the same high frequencies can yield additional insight in this behaviour.

3.5 The central resonance of Ni:Zn(en)$_3$(NO$_3$)$_2$

The central line (C) in the multiplet of Ni:Zn(en)$_3$(NO$_3$)$_2$ in figures 3.3 and 3.4 is not explained by the normal Δm = 1 transitions discussed above. This line was previously attributed to a double quantum resonance [2], but is unusually strong for such a process. We will study this transition in more detail with high frequency EPR measurements.

The parameters for the Ni^{2+} centers can be obtained for both crystallographic phases from the positions of the $S = 1$ resonances. Since the double quantum resonance originates from the same paramagnetic species, the same set of parameters can be used to predict the resonance positions of the double quantum resonance. The predictions are based on the theory that the intensity of the double quantum resonance is stronger when the intermediate state coincides with a real eigenstate [9, 13, 7, 17], although the experiments by Orton *et. al.* also showed a double quantum resonance using 2 different frequencies in which the "mixed" double quantum resonance was situated half way between the two "pure" double quantum resonances [10].

As stated before, only for a limited range of orientations, the intermediate state coincides with a real eigenstate. which is necessary for a strong double quantum resonance to be observed [9]. Assuming the double quantum resonance is detected at the same magnetic field as the magic angle orientation in crystals, it can be calculated using brute force techniques and eq 3.2 to be 6.292 tesla at 190 K / 190 GHz and 6.275 tesla at 115 K / 190 GHz.

A more sophisticated approach is the derivatization of Muha that led to the following formula for calculating under which conditions double quantum resonances occur for a system with an *isotropic* g-factor and no rhombicity [2, 18]:

$$cos^2\theta + cos2\theta = \frac{2D^2}{9(g_e\mu_B B)^2} \tag{3.3}$$

In which D is the zero field parameter and $(g_e\mu_B B)$ is the Zeeman interaction. It is easily verified that for zero field interactions that are small compared to the Zeeman interaction, the angle θ will approach the magic angle of 54.7°. This formula can only be used as an approximation for both the high and low temperature data, since the effect of the anisotropy between the $g_{||}$ and $g_{\perp}$ increases the angle θ from 55.6° to 55.8°.

The calculated central magnetic field values of 6.275 and 6.298 for the resonance above resp. below the phase transition temperature differ only slightly from the observed field of 6.286 ± 0.002 tesla (experimental accuracy) for both temperatures at 190 K. Therefore on the basis of resonant energies the double quantum resonance appears a reasonable explanation, although the predicted shift to lower magnetic field (which is sufficient to be observable in our equipment) is not observed. Furthermore the fine structure of the central peak at both temperatures (fig. 3.5) could not be accounted for with a double quantum resonance based on the parameters obtained from the $S = 1$ resonance for the Ni^{2+} ions [12, 19, 20].

It must therefore be concluded that the strong signal observed in the center of the $S = 1$ multiplet is no double quantum resonance, but a different EPR transition. This conclusion is in line with the observations by Van Dam *et.al.*[1, 2] who observed identical behaviour for single and double quantum resonances, contrary to the quadratic dependence expected. Linear behaviour is more expected from single quantum transitions.

3.6 Discussion

In this section we examine critically a number of possibilities which would allow to explain the central line by a double quantum resonance, while not affecting the interpretation of the single quantum resonances originating from the $S = 1$ ground state of the Ni^{2+} ions.

The effect of the small distribution in the rhombicity term discussed only leads to a slightly more broadened double quantum resonance, but not to the observed (fine) structure. Theoretically the distribution observed in

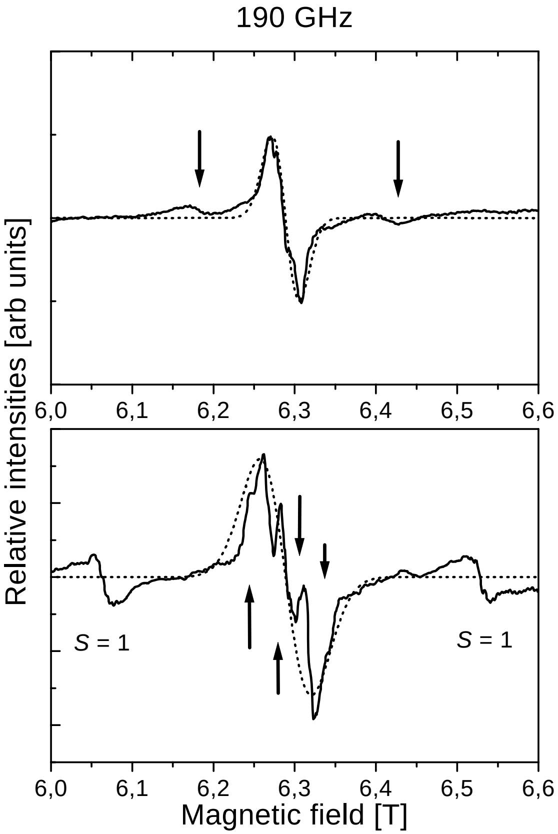

Figure 3.5: The absorption of the central resonance of Ni:Zn(en)$_3$(NO$_3$)$_2$ at 190 GHz and 190 K (top) compared to a double quantum resonance simulation. Although a good fit is achieved for the central signal, the two small signals marked by arrows can not be explained in this way. Lowering the temperature to 115 K clearly shows that the observed fine structure cannot be explained by a double quantum resonance.

the $S = 1$ resonance due to the six inequivalent sites could be sufficiently resolved for the central resonance to be observed. Since only four and not six resonances are observed this is not likely, furthermore in the single crystal experiments these inequivalent sites differed exclusively in their relative orientation. The random distribution in the powder used for the current experiment would average out any orientational effect.

A second possibility is hyperfine splitting of the central line caused by the nuclear spin of the nickel ions. However the only relevant isotope is ^{61}Ni which, with an abundance of less than 2% [21], is too low to make a significant contribution. Although this would theoretically yield identical intensities (1:1:1:1) as has been observed for the central resonance.

A third possible mechanism is the existence of truly inequivalent sites below the phase transition temperature. Based on the crystal structure published by Wilson *et.al.* and Prasad *et.al* [14, 15] this would be a possibility. However based on the crystal structure (fig. 3.6) only two chemically inequivalent sites are expected, which gives rise to a doublet signal and not to the observed fine structure. Moreover the relative differences in either the g-tensor or the zero field parameters need to be quite substantial to explain the magnetic field differences observed in the central resonance. Changing these parameters to yield the observed splittings of the central resonance would also influence the $S = 1$ resonances which would be detected.

In conclusion all realistic double quantum scenarios fail to explain the observed structure of the central resonance. We therefore propose that the central resonance originates from an unexpected paramagnetic center, not necessarily related to the Ni^{2+} ion.

If we assume an arbitrary $S = \frac{3}{2}$ species the transitions can be calculated using equation 3.2 with a small rhombic distortion and zero field splitting. As can be seen in figure 3.7 the 190 K data is in good agreement when the parameters: $g_x = 2.168$, $g_y = 2.160$, $g_z = 2.152$, $D = +0.07$ cm^{-1} and $E = +0.0225$ cm^{-1} are used. Both the overall line shape and the two small side bands adjacent to the central resonance are visible in the simulation. At temperatures below the crystallographic phase transition temperature the g-values are found to remain mostly unchanged: $g_x = 2.168$, $g_y = 2.160$, $g_z = 2.148$, with a zero field splitting that is increased to $+0.15$ cm^{-1} and a rhombic distortion of $+0.05$ cm^{-1}. The two small signals predicted, marked by arrows, are not visible experimentally. The signals can either be obscured by the $S = 1$ multiplet of which the inner transitions at low temperatures are close to the $S = \frac{3}{2}$ multipet, or are spread out by the presence of a distribution in the rhombicity term E. The current data is not sufficient to

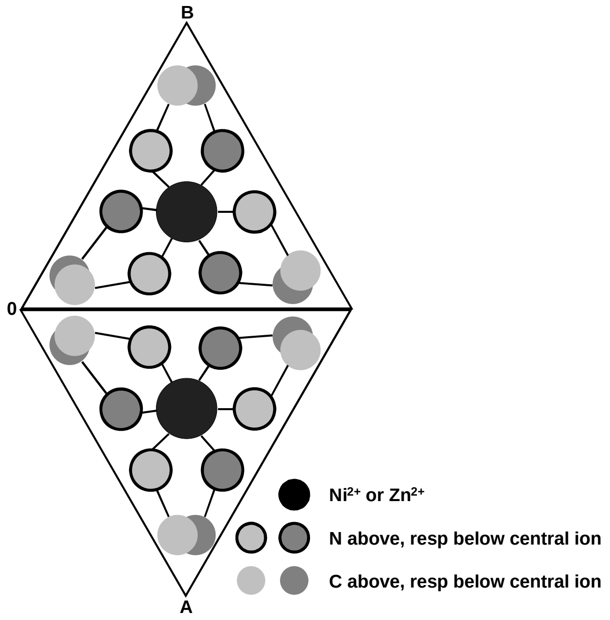

Figure 3.6: The unit cell of Zn(en)$_3$(NO$_3$)$_2$, viewed along the crystallographic c-axis. The NO_3^- groups have been omitted for clarity. All three ligands are in the δ configuration

distinguish between the two effects.

The origin of the assumed $S = \frac{3}{2}$ species remains unexplained. Possibly Ni^{3+}, Zn^{5+} or the inclusion of an unknown $S = \frac{3}{2}$ impurity are responsible. The creation of a stable $S = \frac{3}{2}$ system from one of the ethylene diamines or NO$_3$ groups can be disregarded due to the high reactivity of small organic radicals. The ionization of zinc ions to a 5+ ionization state is unlikely due to the reactivity of such a center and the energies involved. Most probable is the creation of a Ni^{3+} ion, because the Ni^{3+} ion can have a distribution of the $3d$ atomic orbitals to allow for an $S = \frac{3}{2}$ ground state. Nickel ions in the Zn(en)$_3$(NO$_3$)$_2$ matrix have an octahedral ligand field and as a consequence have a $^3A_{2g}$ ground state [16]. In this state the $3d_{xz}$ and $3d_{yz}$ atomic orbitals have the highest energy. The $3d_{x^2-y^2}$ and the $3d_{xy}$ make up the intermediate energy level and the $3d_{z^2}$ has the lowest energy. The relative

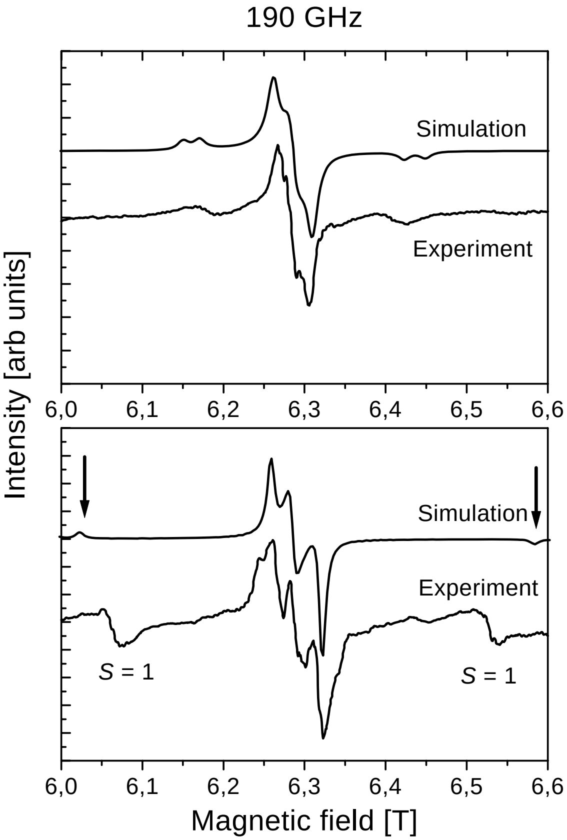

Figure 3.7: Comparison of the high (top) and low (bottom) temperature experimental data at 190 GHz with simulations based on an $S = \frac{3}{2}$ spin state with : $g_x = 2.168$, $g_y = 2.160$, $g_z = 2.152$, D =0.07 cm^{-1} and E =0.0225 cm^{-1} (top). Parameters for the bottom spectrum are $g_x = 2.168$, $g_y = 2.160$, $g_z = 2.148$, $D = 0.15$ cm^{-1} and $E = 0.05$ cm^{-1}.

energies of the energy levels assure that if a nickel ion is oxidized from the 2+ to the 3+ state the spin state is decreased from the $S = 1$ state to the $S = \frac{1}{2}$ state.

For the Ni^{3+} ions to have an $S = \frac{3}{2}$ ground state the energy levels need to change from an ^{3}A$_{2g}$ to an ^{6}A$_1$ system. Such a change can easily be accomplished by a change in the symmetry of the surrounding ligands from octahedral to cubic [22]. In order to have the observed fine structure both an axial and a rhombic distortion need to be present. From the parameters obtained (D and $E \neq 0$ for both crystallographic phases) it can be concluded that this is the case.

Judging by the intensity of the central resonance about 10% of the nickel ions is in an $S = \frac{3}{2}$ spin state. Furthermore the g-values, which are mostly influenced by the central ion, for both the $S = 1$ and the $S = \frac{3}{2}$ paramagnetic species are very much alike, while the zero field splitting which is mostly dependent on the surrounding crystal field is remarkably different [23, sec 2.3]. Therefore the presence of $S = \frac{3}{2}$, Ni^{3+} ground state is highly probable.

The intensity of the central peak suggests that random impurities can hardly be responsible for the signal. In principle an additional NMR or ENDOR study could prove this argument.

3.7 Conclusions

The $S = 1$ resonances of Ni^{2+} ions doped in Zn(en)$_3$(NO$_3$)$_2$ have been measured at temperatures above and below the crystallographic phase transition of Zn(en)$_3$(NO$_3$)$_2$. The g-values in both crystallographic phases are given by $g_{||} = 2.160$ and $g_{\perp} = 2.148$. The zero field splitting is reduced from 0.83 to 0.77 cm^{-1} with the introduction of the rhombic distortion at low temperatures. From the relative intensities within the $S = 1$ multiplet a distribution around 0.10 cm^{-1} was proposed.

The behaviour and the shape of the signal in the center of the $S = 1$ multiplet can not be explained by a double quantum resonance, or enhanced consecutive single quantum resonances. The single quantum transitions of an $S = \frac{3}{2}$ spin state are found to be a good explanation. This spin state most likely originates from a Ni^3+ ion in a cubic ligand field.

Bibliography

[1] P.J. van Dam, A.A.K. Klaassen, E.J. Reijerse, and W.R. Hagen. Application of high frequency EPR to integer spin systems: Unusual behaviour of the double-quantum line. *J. Magn. Res.*, 130:140–144, 1998.

[2] P.J.M. van Dam. *Multifrequency EPR studies on Biological systems.* PhD thesis, University of Nijmegen, 1998.

[3] S. Saxena and J.H. Freed. Double quantum two-dimensional Fourier transform electron spin resonance: distance measurements. *Chem. Phys. Lett.*, 251:102–110, 1996.

[4] S. Saxena and J.H. Freed. Theory of double quantum two-dimensional electron spin resonance with application to distance measurements. *J. Chem. Phys.*, 107:1317–1339, 1997.

[5] P.P. Borbat and J.H. Freed. Multiple-quantum ESR and distance measurements. *Chem. Phys. Lett.*, 313:145–154, 1999.

[6] M. Katayama. Double quantum transition in electron spin resonance of gamma irradiated acetyl-d,l-alanine. *Phys. Rev*, 126:1440–1442, 1962.

[7] P.P. Sorokin, I.L. Gelles, and W.V. Smith. Multiple quantum transitions in paramagnetic resonance. *Phys. Rev.*, 112:1513–1515, 1958.

[8] S.C. Ke and H.T.Tohver. Double quantum transitions of Mn^{2+} in CaO. *J. Phys. :Condens. Matter*, 6:8331–8334, 1994.

[9] M. Göppert-Mayer. über elementarakte mit zwei quantumsprüngen. *Ann. Phys.*, 9:273–294, 1931.

[10] J.W. Orton, P. Auzins, and J.E. Wertz. Double quantum electron spin resonance transitions of nickel in magnesium oxide. *Phys. Rev. Lett.*, 4:128–129, 1960.

[11] S.R.P. Smith, F. Dravnieks, and J.E. Werz. Electron paramagnetic resonance lineshape of Ni^{2+} in MgO. *Phys. Rev.*, 178:471–480, 1969.

[12] J.W. Orton, P. Auzins, J.H.E. Griffiths, and J.E. Wertz. Electron spin resonance studies of impurity ions in magnesium oxide. *Proc. Phys. Soc. A.*, 78:554–568, 1981.

[13] M.S. De Groot and J.H. van der Waals. The two quantum transition in the electron resonance spectrum of phosphorescent aromatic hydrocarbons. *Physica*, 29:1128–1132, 1963.

[14] L. Sreeramanchandra Prasad and S. Subramanian. Zero field tensor for NiII in Zn(ethylenediamine)$_3$ $(NO_3)_2$: EPR study. *J. Chem. Phys.*, 88:43–45, 1988.

[15] D. Neill, M.J. Riley, and C.H.L. Kennard. Tris(ethylenediamine-N,N')zinc(II) Dinitrate. *Acta. Chrys.*, C53:701–703, 1997.

[16] C.R. Wilson, M.J. Riley, D. Wang, and G.R. Hanson. Electron paramagnetic resonance of Ni(II) doped tris(ethylenenediamine)zinc(II) dinitrate. *Chem. Phys.*, 217:63–70, 1997.

[17] C.C. McDonald. Multiple-quantum transitions in EPR spectra of atomic oxygen. *J. Chem. Phys*, 39:3159–3160, 1963.

[18] G.M. Muha. The Zeeman effect in spin = 1 systems. *J. Magn. Res.*, 49:431–443, 1982.

[19] P. Kottis and R. Lefebvre. Calculation of the electron spin resonance line shape of randomly orientated molecules in a triplet spin state, I. the Δm = 2 transition with a constant linewidth. *J. Chem. Phys.*, 39:393–403, 1963.

[20] P. Kottis and R. Lefebvre. Calculation of the electron spin resonance line shape of randomly orientated molecules in a triplet spin state,

II. the correlation of the spectrum with the zero-field splittings. introduction of an orientation-dependent linewidth. *J. Chem. Phys.*, 41:379–393, 1964.

[21] F.W. McLafferty and F. Turecek. *Interpretation of mass spectra, fourth edition.* University Science Books, 1993.

[22] J.E. Huheey. *Inorganic chemistry: Principles of structure and reactivity, third edition.* Harper Collins, 1983.

[23] J.W. Orton. *Electron Paramagnetic Resonance, an introduction to transition group ions in crystals.* London Ilife Books LTD, 1968.

Chapter 4

The magnetic ground state of manganocene

Abstract

We have studied the pure solid state of $\mathrm{Mn(C_5H_5)_2}$ with magnetization and EPR experiments. The magnetization was found to be nearly independent of temperature and linear with magnetic field. The magnetic susceptibility resembles antiferromagnetic coupling, but at magnetic fields above 5 tesla paramagnetic like behaviour is observed.

In the EPR spectra two separate resonances are observed, with intensity varying with temperature and field. Namely an $S = \frac{5}{2}$ state with a zero field splitting of around 0.20 cm^{-1} while the other resembles an $S = \frac{1}{2}$ transition. The large dependence of the g-value on temperature for this resonance from $g = 2.0023$ (up to 10%) is indicative of an antiferromagnetic resonance.

We explain the ground state by an $S = \frac{5}{2}$ energy spectrum with an antiferromagnetic coupling at low temperatures. The additional resonance in the EPR spectra originates from an antiferromagnetic resonance in the quasi 1-dimensional chains. The exchange interaction resulting in this coupling leads at intermediate fields to a level crossing, thereby returning the system to a paramagnetic ground state.

4.1 Manganocene as an unusual metallocene

Metallocene chemistry started with the synthesis of *"Ferrocene"*[1] by Kealy and Pausson [3]. The Grignard reaction between cyclopentadienylmagnesium and ferric chloride yielded, instead of the desired fulvalene, a compound with structural formula $FeC_{10}H_{10}$. Failure of earlier workers to prepare similar compounds, and the remarkable stability, led the authors to believe that their success had to be attributed to the tendency of the cyclopentadienyl groups to become aromatic by acquisition of an additional electron. The structure they proposed is drawn in figure 4.1(B).

Barely four months after the publication of the planar dicyclopentadienyl-iron structure, Wilkinson and coworkers proposed two structures in which all five carbon atoms of the cyclopentadienyl rings were bonded to the central ion [4]. The proposed structures were more in accordance with their IR-measurements, showing only one type of C-H bond. Although the prismatic structure, such as might result from a split d^3 p^2 plane pentagonal bonding was not excluded, the anti-prism structure was believed to have

---

[1] The name Ferrocene, and the generic name metallocene, was first coined by M. Whiting [1, 2], who showed that these compounds could be considered as a new type of aromatic system. The name emphasizes the analogy with benzene.

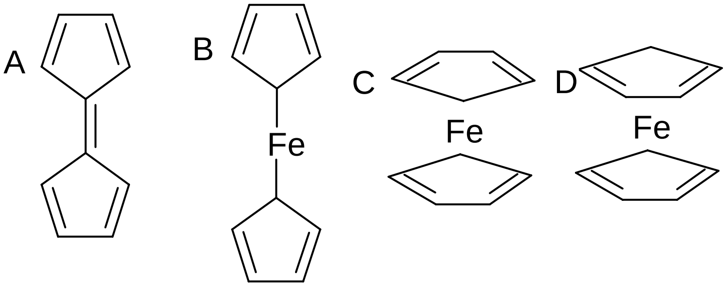

Figure 4.1: (A) The stucture of fulvalene that Kealy and Pausson intended to synthesize, and (B) the iron compound they thought resulted. (C) and (D) are the anti-prism and prismatic structure respectively.

a lower energy. The correctness of the anti-prism structure[2] was proven in 1953 based on X-ray crystallography [5].

The unusual properties of the metallocenes, and the relative ease with which a large number of transition metals could be inserted in a wide variety of substituted aromatic (ring)-species led to a large interest in this field of synthetic chemistry. The review article by Pausson [6] already shows a wide variety in both the central ions and (alkylated-) ring systems. Quite soon it was discovered that metallocenes were good fuel additives, which triggered new interest in these compounds [7]. The third wave of interest came as it was discovered that metallocene-like compounds, in which one of the aromatic rings is replaced with a number of CO-groups, were good candidates for heterogenic catalyses. It is in this field that most research concerning metallocenes is currently conducted, although emphasis is now shifting to homogenic catalyses, reducing the number of papers on metallocenes.

4.1.1 Structural anomaly of Manganocene

The metallocenes with a Mn^{2+} or Pb^{2+} ion in the center of 2 cyclopentadienyl anions, are the only known *pure* metallocenes that do not crystallize in a staggered configuration, but in quasi 1-dimensional chains [8, 9]. In 1978 Bünder and Weiss showed that the room temperature crystal of manganocene is made up of polymer chains with a zig-zag arrangement (rhombic modification) of MnC_5H_5 units, bridged by C_5H_5 rings between adjacent manganese ions, see figure 4.2. Calculations suggested that the bridging cyclopentadienyl rings are tilted at an angle of 65 degrees with respect to the manganese-manganese vector. The tilted geometry favors a crystal molecular orbit in which the bridging cyclopentadienyl rings are bonded with two carbon atoms to one (η_2 interaction), and with three carbon atoms to the other (η_3 interaction) manganese ion in the quasi 1-dimensional chain [10].

The rhombic modification is reported to be stable up to the transition temperature of 432 K, above which the quasi 1-dimensional chain breaks up. The solid is made up of individual $Mn(C_5H_5)_2$ units in the staggered

---

[2] Nowadays the nomenclature is changed to *staggered* and *eclipsed*, analogous with the nomenclature of side-groups along a molecular axis.

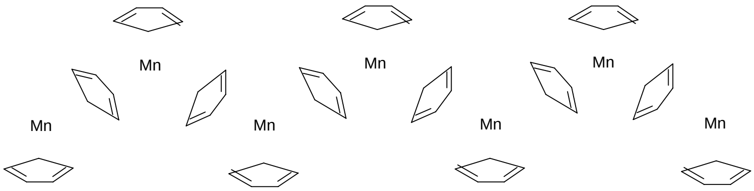

Figure 4.2: The Rhombic modification of manganocene in the pure solid reproduced from [8].

configuration, identical to other metallocene solids. The staggered configuration is stable up to the melting point of 445 K.

4.1.2 The magnetic ground state of manganocene

Most neutral metallocenes are diamagnetic and have no measurable magnetization. Manganocene is an exception, with five electrons populating the manganese *d* orbitals. Theoretically both a high- or a low-spin arrangement are possible. The arrangement of the electrons over all 5 *3d* orbitals of the manganese ions is expected to be the most favorable, leading to a paramagnetic $S = \frac{5}{2}$ ground state. Magnetization measurements show that pure manganocene behaves anti-ferromagnetically at low temperatures [11, 12, 13, 14].

From experiments on manganocene, both in the gas phase and when diluted in host lattices, it is known that not always the expected ground state is observed. Experimentally it has been shown that both high-spin and low-spin spectra can be seen under similar conditions in a host matrix [13, 15, 16]. Furthermore experiments performed on the gas phase of $\mathrm{Mn(C_5H_5)_2}$ showed the existence of an equilibrium between the high-spin and low-spin configurations at slightly elevated temperatures [17]. The exact position of these equilibria is dependent on both the temperature and the amount of ring alkylation. In $\mathrm{Mn(C_5H_5)_2}$ the ground state is predominantly $S = \frac{5}{2}$, while the fully methylated $\mathrm{Mn(C_5(CH_3)_5)_2}$ is predominantly $S = \frac{1}{2}$ [14].

As an extension of the gas phase equilibrium it was demonstrated that the crystal structure of the host lattice also has a profound influence on the spin state. Depending on the size of the substituted lattice sites the $Mn(C_5H_5)_2$ molecules are either high-spin or low spin. The high-spin configuration is occurring in *large* lattice sites [15, 16], while the low-spin configuration occurs in lattice sites were the $Mn(C_5H_5)_2$ molecules are *compressed*. In a number of hosts the size is such that an equilibrium can be observed. The occurrence of these equilibria in $Mn(C_5H_5)_2$ is stated to be the only known example for high- and low-spin Mn^{2+} ions in a solid [11].

Using multifrequency EPR experiments in combination with magnetization measurements over a broad range of both temperature and magnetic field we study the (magnetic) ground state of pure $Mn(C_5H_5)_2$.

4.2 Experimental methods

$Mn(C_5H_5)_2$ was purchased from "*Brunswich Chemie*" in Amsterdam and used without further purification. $Mn(C_5H_5)_2$ is very sensitive to air (pyrophore) and reactive towards metals (strong oxidizer). Due to this reactivity towards metals a non-metallic, non-resonant EPR-sample holder was constructed consisting of a quartz capillary with a metal coating on the outside to contain the microwave radiation. For mechanical strength the capillary was mounted in a polyethylene cylinder. Magnetization measurements were performed in an airtight nylon[3] sample holder.

All samples were loaded under a nitrogen atmosphere and sealed with a polyethylene stopper. The sample holders were transferred to the helium atmosphere of the respective flow cryostat for EPR or magnetization measurements in the shortest time possible. During transport the sample holders were kept in liquid nitrogen to avoid oxidation or contamination.

The magnetization was measured with a "single shot" magnetometer. The sample holder was weighed before and after loading to determine the amount of metallocene present. X-band EPR measurements were recorded on a Bruker spectrometer. High frequency EPR measurements were recorded with the HF-EPR set-up described in section 2.4.

---

[3] Trade name Kel-f

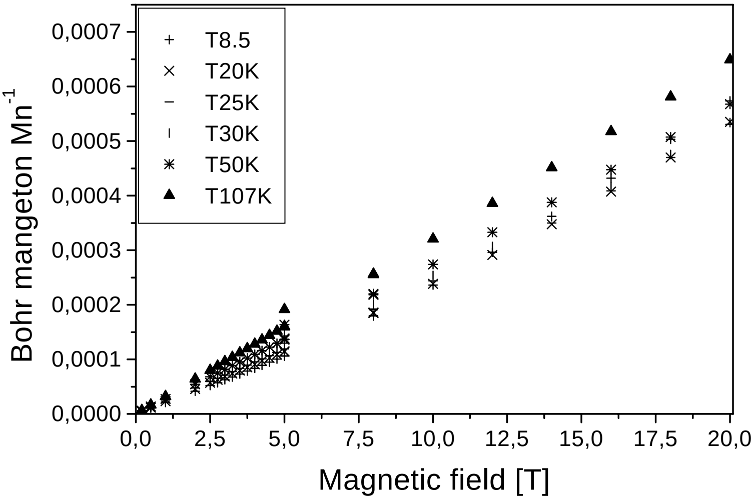

Figure 4.3: The measured magnetization of Mn(C_5H_5)$_2$ as function of both temperature and field expressed in Bohr magneton per manganese ion. Not only is the magnetization nearly linear in magnetic field, the dependence on temperature is very uncharacteristic.

4.3 Magnetization measurements of manganocene

The magnetization of Mn(C_5H_5)$_2$ was measured between 8.5 and 110 K, and from 0.1 to 20 T (fig. 4.3). The observed magnetization is essentially linear with respect to the magnetic field and nearly independent of the temperature (fig. 4.3). The low maximum magnetization excludes a pure $S = \frac{1}{2}$ or $S = \frac{5}{2}$ ground state.

The magnetization divided by the magnetic field as an approximation to the magnetic susceptibility [18], is shown in figure 4.4. The stronger decrease of the susceptibility at lower temperatures is consistent with antiferromagnetism. On the other hand the behaviour in magnetic fields above 5 tesla cannot be explained this way. In addition the susceptibility remains non-zero. We therefore propose that at low temperatures an antiferromagnetic coupling between the manganocene units is observed, while at higher

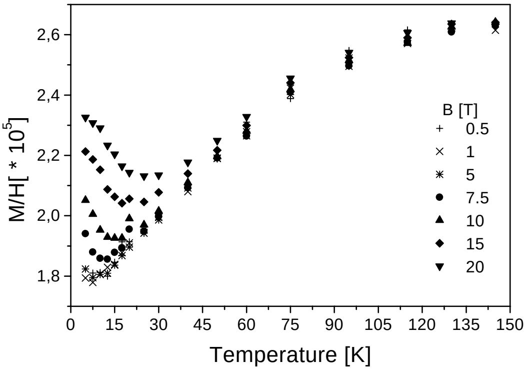

Figure 4.4: The field and temperature dependence of the magnetic susceptibility of manganocene. The low field measurements indicate an antiferromagnetic coupling, but the data above 5 tesla indicates the presence of additional paramagnetic impurities.

magnetic fields observations are made that can be interpreted as the onset of paramagnetic behaviour. The magnetization experiments do not allow to conclude whether this phase-change causes the destruction of the antiferromagnetic coupling, whether the formation of a new magnetic species (dimer or long range interaction) appears, or whether merely a different magnetic ground state appears. This last is believed to be the most likely due to the small difference between the $S = \frac{1}{2}$ and the $S = \frac{5}{2}$ spinstate of the manganese ion.

4.4 (HF)-EPR measurements on manganocene

4.4.1 $S = \frac{5}{2}$ resonances

At 12 K the X-band EPR shows a small signal at low field with respect to the main resonance. This small signal is a multiplet reminiscent of an $S = \frac{5}{2}$ spin. At 30 K the multiplet is reduced to a shoulder and at higher temperatures it becomes unobservable (fig. 4.5).

High frequency EPR at 12 K shows a strong high field signal with

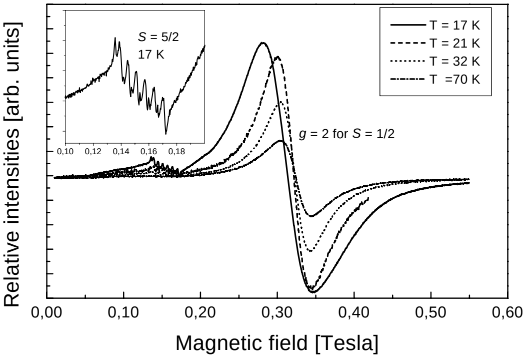

Figure 4.5: X-band EPR spectra of manganocene at various temperatures. Only at the lowest temperatures an $S = \frac{5}{2}$ signal can be observed alongside the broad resonance at $g \approx 2$ for an $S = \frac{1}{2}$ system.

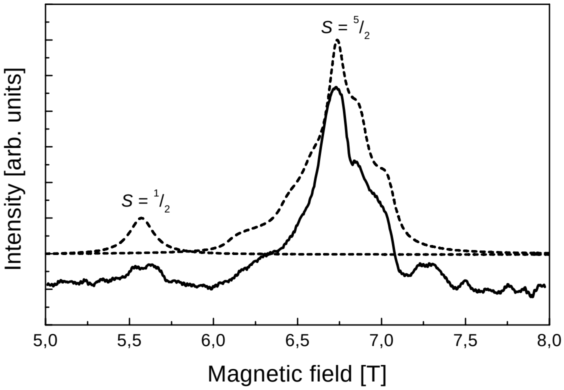

Figure 4.6: The two resonances of Mn(C_5H_5)$_2$ at 12 K and 190.31 GHz fitted with an $S = \frac{1}{2}$ and an $S = \frac{5}{2}$ spin state respectively.

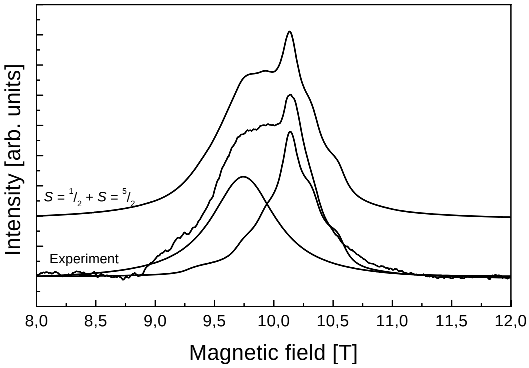

Figure 4.7: Experimental data at 31 K and 285 GHz compared to a superposition of an $S = \frac{1}{2}$ and an $S = \frac{5}{2}$ simulation. The two traces under the experimental trace are the individual $S = \frac{1}{2}$ and $S = \frac{5}{2}$ resonances.

some fine structure and a weak low field signal (fig. 4.6). Around 30 K the fine structure becomes less pronounced, while the low field signal has shifted sufficiently to higher field to be observable as a shoulder on the high field signal (fig. 4.7), while at 70 K the distinction between the two peaks disappears. Further increase of the temperature narrows down the only remaining signal (fig. 4.8).

Based on equilibrium theory (see 4.1.2) the presence of an $S = \frac{5}{2}$ spin state is a safe starting point. The multiplet in the X-band spectra at 12 K and the fine structure of the main resonance in the 190 GHz spectrum can be described by using Hamiltonian 4.1:

$$\mathcal{H} = \mu_B \overrightarrow{B} \overline{\overline{g}} \overrightarrow{S} + D \left[S_z^2 - \frac{S(S+1)}{3} \right] \tag{4.1}$$

with $g_{iso} = 2.0$ and $D =$ -0.24 cm^{-1}. As temperature is increased the zero field splitting decreases up to -0.04 cm^{-1} for an $S = \frac{5}{2}$ signal at 106 K. Since identical results are obtained under different conditions the assumption of an $S = \frac{5}{2}$ spin state is valid.

4.4.2 The $S = \frac{1}{2}$ like resonance

In the X-band spectra at all temperatures a strong resonance can be seen at the magnetic field value for an $g_{iso} = 2$, $S = \frac{1}{2}$ spin system (fig. 4.5). The increase in temperature leads to a reduced height in the first derivative signal and a small shift towards high magnetic field.

In the high frequency spectra at low temperatures a small low field signal is observed, that does not display fine structure (fig. 4.6). As the temperature increases this resonance can be seen to shift towards higher field values until it finally is superimposed with the $S = \frac{5}{2}$ signal described above (fig. 4.8).

Assuming an equilibrium and based on the X-band data and the absence of fine structure in the high frequency data, it is reasonable to expect an $S = \frac{1}{2}$ spin system. However the very broad signal and the extreme temperature dependence in both the X-band and high frequency data should caution us. The g-values determined from fitting the high frequency data are summarized in figure 4.9. Clearly the difference in temperature dependence between the $S = \frac{5}{2}$ and the assumed $S = \frac{1}{2}$ state can be seen. Shifts of the g-value with the strength demonstrated by the alleged $S = \frac{1}{2}$ state

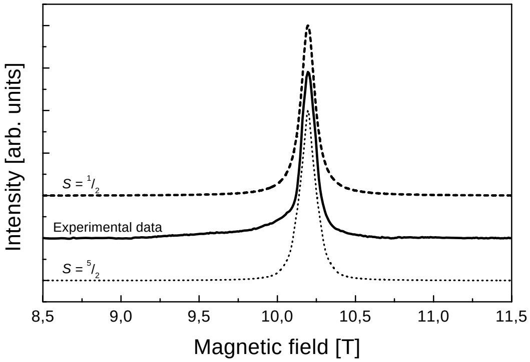

Figure 4.8: The 106 K EPR spectrum of manganocene at 285.46 GHz compared to simulations of both an $S = \frac{1}{2}$ and an $S = \frac{5}{2}$ spin system.

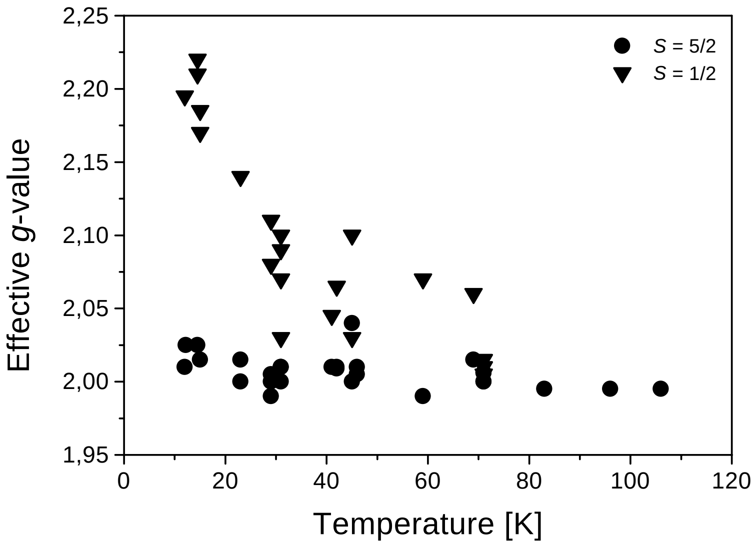

Figure 4.9: The observed g_{iso} of the resonances in $Mn(C_5H_5)_2$ at various temperatures and EPR frequencies.

(up to 10%) are very uncommon for an EPR transition.

Together with the observed behaviour in the magnetic susceptibility this leads us to question the validity of an equilibrium between an $S = \frac{1}{2}$ and an $S = \frac{5}{2}$ spin state. The presence of an $S = \frac{5}{2}$ spin state is confirmed by the consistency with which high and low frequency EPR data point to the same parameters for the isotropic g-value and the zero field splitting. The $S = \frac{1}{2}$ like resonance on the other hand does not appear to originate from an EPR transition. In the next section we try to explain the data by assuming an anti-ferromagnetic resonance.

4.5 Antiferromagnetic resonance of manganocene

We will restrict ourselves to the general trends of an antiferromagnetic resonance in our attempt to identify the anomalous resonance as an antiferromagnetic resonance. Explaining the $S = \frac{1}{2}$ like resonance as an antiferromagnetic resonance of the $S = \frac{5}{2}$ spin state, together with the observed behaviour in the magnetization experiments would be proof of a single $S = \frac{5}{2}$ ground state at low temperatures.

4.5.1 General antiferromagnetic resonance

The investigation of antiferromagnetic resonance in magnetic materials is generally performed using the same experimental conditions (high frequency radiation in the presence of high magnetic fields) as EPR techniques. Usually the large differences in resonance conditions prevent a confusion of interpretation between an anti-ferromagnetic and an electron paramagnetic resonance.

An antiferromagnetic material can be thought to exist of two sublattices. Each sublattice has a net magnetization, but overall the magnetic fields cancel each other out. Both sublattices may be supposed to be subject to an exchange field (B_e) proportional to the magnetization of the other sublattice as well as to anisotropy fields (B_k). The secular equation for this configuration is:

$$\omega_0^2 = \gamma^2(B_k^2 + 2B_eB_k) \tag{4.2}$$

assuming $B_e \gg B_k$ with the exchange field common to both sublattices equation 4.2 becomes:

$$\omega_0 \sim \gamma(2B_eB_k)^{\frac{1}{2}} \tag{4.3}$$

Antiferromagnetic resonance occurs at these frequencies even in the absence of applied fields. With applied fields the modified calculations lead to:

$$\omega_0 = \gamma B_0 \pm \gamma(B_k^2 + 2B_eB_k)^{\frac{1}{2}} \tag{4.4}$$

The equation describes conditions for which an applied field / frequency combination causes spin flopping or reordering of the spins in a direction normal to the original axis, when the temperature is below the Néel temperature. Typically the resonance condition is in the order of a few gigaherz. Reducing the temperature towards absolute zero increases the resonance frequency. The rate of increase diminishes with temperature and is nil at absolute zero.

4.5.2 Antiferromagnetic resonance of quasi 1-D systems

The pure metallocene Mn(C_5H_5)$_2$ is structurally very similar to the known quasi 1-D (one dimensional) linear antiferromagnets $(CH_3)_4NMnCl_3$, $(CH_3)_2NH_2MnCl_3$ and $CsMnCl_3{\cdot}2H_2O$ (and the analogue $CsMnCl_3{\cdot}2D_2O$). In each of these materials, for structural reasons, dominant super exchange coupling between Mn^{2+} ion occurs in -$MnCl_n$- chains which extend in specified directions of the crystals and are magnetically insulated from each other by the intermediate atoms [19, 20]. This situation is comparable to the manganocene chain in which the Mn^{2+} ions are magnetically separated by cyclopentadienyl rings.

Temperature dependent experiments on these materials at microwave frequencies showed anomalously large shifts of (assumed) paramagnetic resonance lines when the temperature was reduced and the Néel temperature was approached. All microwave experiments on the quasi 1-D antiferromagnets show similar behaviour when the temperature is lowered. Well above the Néel temperature the magnetic resonance does not shift. While the temperature approaches the Néel temperature a sharp increase of the *effective* g-value (up to 10%) is observed [19, 20, 21, 22].

The predicted behaviour with magnetic field and temperature for these 1-D systems is comparable to the behaviour of the anomalous signal in the high frequency EPR spectra. At high temperatures this resonance is not existent or it is completely swamped by the relatively temperature independent resonance of the $S = \frac{5}{2}$ spin state.

The observations reported in sections 4.3 and 4.4 are in good agreement with an antiferromagnetic resonance. The observations of EPR spectra at temperatures as low as 12 K in an antiferromagnetic ground state can either be due to the existence of non-magnetically-interacted area's in the powder, or of a magnetic phase transition back to a paramagnetic ground state at high magnetic field. The driving force behind the phase transition is the decrease of energy associated with the $S = \frac{5}{2}$ energy level in high magnetic field, making the paramagnetic state more favorable than the antiferromagnetic state. Such a field dependent reversal in the magnetic ground state is visible in the magnetic susceptibility data presented in figure 4.4.

4.6 Discussion

Although long-range anti-ferromagnetic resonance can account for the observed effects, we now attempt to obtain the same result by incorporating pair interaction effects.

The influence of pair interactions on observed EPR spectra and magnetization experiments can be quite considerable. The structure of manganocene can be compared to those of the so-called "*ladder*" compounds. In such ladder compounds the formation of spin pairs (as the rungs of a ladder) is possible. Spin pair formation for the manganocene had already been investigated by Köning *et.al.* to achieve a good fit between their theoretical models and the magnetization data of Mn(C_5H_5)$_2$ obtained at low field and low temperatures [12]. The difference between the isolated pair model and the Heisenberg linear chain model they favored is very small. Both models are based on an $S = \frac{5}{2}$ spin with an isotropic g-value of 2. The interaction energy $(\frac{J}{k})$[4] of the isolated pair model is 22.5 K, while the antiferromagnetic Heisenberg linear chain has an interaction energy $(\frac{J}{k})$ of 14 K with an interchain correction factor of 5 K.

4.6.1 EPR active dimer systems

Individual atoms may be coupled anti-parallel leading qualitatively to the observed behaviour in the magnetization, but cannot explain the detection of EPR. Alternatively parallel coupling leads to an $S = 5$ system with a large zero field splitting, depending on the interaction energy, which could be observable in EPR but could not explain the magnetization data.

To explain the data with an $S = 5$ spin system and an effective g-value of 2.00 the zero field splitting was adjusted until the observed experimental signal was reproduced. The best agreement was achieved with D = -135 cm^{-1}. To shift the same resonance to an effective g-value of 2.20

---

[4] J is the energy of interaction between adjacent spins in the quasi 1-D chains. For ease of comparison it is divided by the Boltzman constant k to yield an energy expressed in K.

at 12 K D had to be adjusted to about -105 cm^{-1}. However, at low temperatures the distances between the manganocene units is decreased, leading to an increased overlap of the wave functions between the Mn^{2+} $3d$ orbitals and the π orbitals on the cyclopentadiene rings. The increase of the overlap would result in an increase of the interaction energy, and hence of the zero field splitting. Furthermore the magnetization behavior would be ferromagnetic, instead of the observed anti-ferromagnetic behaviour. Therefore short-range spin coupling limited to the formation of dimer systems is unlikely to be the cause of the observations made in EPR and magnetization.

4.7 Conclusion

The magnetization per manganese ion is found to be almost linear with magnetic field and nearly independent of temperature in the range 10 to 100 K. Due to the low absolute values at maximum field and minimum temperature it cannot be said whether it is an $S = \frac{1}{2}$ or an $S = \frac{5}{2}$ spin system. The magnetic susceptibility decreases with decreasing temperature as one would expect from an antiferromagnetically coupled system. At fields above 5 tesla the magnetic susceptibility increases at temperatures below 20 K. This behaviour suggests that the sample is restored to the paramagnetic ground state.

The low temperature (< 20 K) X-band EPR spectra show a weak multiplet at $g_{eff} = 4.2$. The position and hyperfine structure are consistent with an Mn^{2+}, $S = \frac{5}{2}$ spin system with $g_{iso} = 2.0$ and $D =$ -0.24 cm^{-1}. The spectra are however dominated by a broad feature at $g_{iso} \approx 2$. As the temperature increases the weak signal becomes unobservable while the dominant signal narrows down and decreases in intensity.

High field, high frequency EPR at low temperatures (around 12 K) show a strong signal with structure consistent with an Mn^{2+}, $S = \frac{5}{2}$ state with a small zero field splitting ($D \approx$ -0.20 cm^{-1}). Furthermore a weak (low field) signal is observed at $g_{eff} = 2.20$. As the temperature is increased the low field signal shifts towards higher field and blends with the $S = \frac{5}{2}$ resonance at $g_{eff} = 2.00$. Simultaneously the observed fine structure on the $S = \frac{5}{2}$ resonance becomes less pronounced due to a reduction of the zero field splitting. At temperatures above 100 K the remaining (single) resonance is equally well described by an $S = \frac{5}{2}$ as an $S = \frac{1}{2}$ spin state. The shift in g-value of the low field signal in the temperature range 12 to 100 K is of the order of 10%, much more than one would expect for strongly influenced paramagnetic systems. The overall tendency is in accordance with an antiferromagnetic resonance and we propose that the low field signal originates from the AFMR resonance of the quasi-1-dimensional chains.

Based on the magnetic phase transition at 5 tesla and the relative intensities of the antiferromagnetic and the EPR resonance in the EPR spectra the small exchange leading to antiferromagnetic behaviour is estimated to be in the order of 13 cm^{-1}. This value is both consistent with the exchange energy as predicted by König *et.al* [12] and with the temperature below which the magnetic phase changes occur.

By assigning the anomalously behaving resonance to an antiferromagnetic resonance no evidence is found for a high-spin low-spin equilibrium in the ground state of pure $\mathrm{Mn(C_5H_5)_2}$. The ground state is determined by the EPR spectra to be $S = \frac{5}{2}$ with a zero field splitting in the order of -0.20 cm^{-1}. The shifts that have been noted in the zero field splitting at various temperatures are most probably due to the shortening of the manganese-manganese vector. This increases the η_3 and η_2 overlap with the neighboring cyclopentadienyl rings. The increasing overlap in return influences the zero field energy of the manganese 3_d orbitals.

At low temperatures an exchange interaction leads to a weak antiferromagnetic coupling. At a magnetic field of about 5 tesla a magnetic phase transition occurs, overcoming the antiferromagnetic exchange and favoring the paramagnetic ground state.

Bibliography

[1] G. Wilkinson. The iron sandwich. A recollection of the first four months. *J. Organom. Chem.*, 100:273–278, 1975.

[2] R.B. Woodward, M. Rosenblum, and M.C. Whiting. A new aromatic system. *J. Am. Chem. Soc.*, 74:3458–3459, 1952.

[3] T.J. Kealy and P.L. Pauson. A new type of organo-iron compound. *Nature*, 168:1039–1040, 1951.

[4] G. Wilkinson, M. Rosenblum, M.C. Whiting, and R.B. Woodward. The structure of iron bis-cyclopentadienyl. *J. Am. Chem. Soc*, 74:2125–2126, 1952.

[5] J.D. Dunitz and L.E. Orgel. bis-cyclopentadienlyl iron: A molecular sandwich. *Nature*, 171:121–122, 1953.

[6] P.L. Pauson. Ferrocene and related compounds. *Quart. Rev.*, 9:391–414, 1955.

[7] M. Rausch, M. Vogel, and H. Rosenberg. Ferrocene: A novel organometallic compound. *J. Chem. Edu.*, 34:268–272, 1957.

[8] W. Bünder and E. Weiss. Die kristallstruktur von bis(cyclopentadienyl)mangan, eine polymere verbindung mit cyclopentadienyl-brücken. *Z. Naturforsch.*, 33 b:1235–1237, 1978.

[9] C. Panattoni, G. Brombieri, and U. Croatto. Ab initio structure determination of two polymorphs of cyclopentadienylrubidium in a single powder spectrum. *Acta Crys.*, 21:823–826, 1966.

[10] E. Canadell, O. Eisenstein, and T. Hughbanks. Electronic switching of ring orientation in cyclopentadienyl-bridged polymers. *Inorg. Chem.*, 23:2435–2440, 1984.

[11] M.E. Switzer, R. Wang, M.F. Rettig, and A.H. Maki. On the electronic ground states of manganocene and 1,1'-dimethylmanganocene. *J. Am. Chem. Soc.*, 96:7669–7674, 1974.

[12] E. König, V.P. Desai, B. Kanellakopoulos, and R. Klenze. Magnetic properties of the quasi one-dimensional heisenberg linear chain antiferromagnet: Manganocene. *Chem. Phys.*, 54:109–113, 1980.

[13] J.L. Robbins, N.M. Edelstein, S.R. Cooper, and J.C. Smart. Synthesis and electronic structures of decamethylmanganocenes. *J. Am. Chem. Soc.*, 101:3853–3857, 1979.

[14] J.C. Smart and J.L. Robins. A low spin manganocene and its novel anionic derivative. Synthesis and characterization of decamethylmanganocene complexes. *J. Am. Chem. Soc.*, 100:3936–3937, 1978.

[15] J.H. Ammeter. EPR of orbitally degenerate sandwich compounds. *J. Magn. Reson.*, 30:299–325, 1978.

[16] J.H. Ammeter, R. Buchner, and N. Oswald. On the high-spin - low-spin equilibrium of manganocene and dimethylmanganocene. *J. Am. Chem. Soc.*, 96:7833–7835, 1974.

[17] J.W. Rabalais, L.O. Werme, T. Bergmark, L. Karlsson, M. Hussain, and K. Siegbahn. Electron spectroscopy of open-shell systems: spectra of $Ni(C_5H_5)_2$, $Fe(C_5H_5)_2$, $Mn(C_5H_5)_2$, and $Cr(C_5H_5)_2$. *J. Chem. Phys.*, 57:1158, 1972.

[18] D. Craik. *Magnetism, principles and apllications.* John Wiley & sons, 1995.

[19] J. Tuchendler, J. Magarino, and J.R. Renard. EPR experiments in the one dimensional salt $(CH_3)_4NMnCl_3$ (TMMC) at temperatures between 4.2 and 70 K. *Phys. Rev. B*, 20:2637–2642, 1979.

[20] K. Nagata and Y. Tazuke. Short range order effects on EPR frequencies in heisenberg linear chain antiferromagnets. *J. Phys. Soc. Japan*, 32:337–345, 1972.

[21] T. Ishii and I. Yamada. Temperature dependence of the width and the frequency of the EPR lines in a one-dimensional Heisenberg antiferromagnet with a Dzyaloshinsky-Moriya antisymmetric exchange interaction as main pertubation term. *J. Phys. Cond. Matt.*, 2:7339–7343, 1990.

[22] H. Okamoto and T. Karasudani. On temperature dependence of EPR frequencies in pseudo-one-dimensional Heisenberg magnets. *J. Phys. Soc. Japan*, 42:717–718, 1977.

Chapter 5

The magnetic ground state of molecular oxygen

Abstract

The magnetic ground state of solid molecular oxygen at low temperatures was never fully understood. For pure oxygen a rigid magnetic ground state consisting of an $S = 1$ triplet with a fixed zero field splitting is assumed. No EPR of oxygen diluted in a host matrix at temperatures above 25 K is published, because of the decrease of the EPR signal with temperature which was generally attributed to line broadening. However recently it has been shown that the local, magnetic moment of individual oxygen molecules in solid oxygen exhibits a steplike discontinuity at the crystallographic $\alpha \rightarrow \beta$ phase transition at 25 K, and therefore the loss of signal may have a deeper reason.

Our high frequency EPR data show that, simultaneous with the disappearance of the spin triplet states, a reduction of the zero field splitting is observed. This reduction of the zero field splitting, together with the vanishing $S = 1$ states, can be seen as a prelude to a change of the ground state.

Furthermore a broad quasi-continuum was observed that persisted at temperatures where the $S = 1$ resonances become undetectable. This quasi-continuum narrows down from 5 to 2 tesla with increasing temperature and becomes more pronounced.

The quasi-continuum originates from two unpaired electrons of molecular oxygen in an uncorrelated state, resulting from a perturbation of the $S = 1$ state. The general low temperature physical and chemical properties of molecular oxygen in view of such a change in the ground state are discussed.

5.1 Introduction

5.1.1 A short history of oxygen

Oxygen is the third most abundant element on earth. In one form or another it makes up for nearly $\frac{1}{2}$ of the earth's crust, roughly $\frac{2}{3}$ of the human body and $\frac{1}{5}$ of the air we breathe [1]. Despite it's relative abundance it is one of the more difficult elements to identify. Although the first methods of oxygen preparation date back to the early 18th century, none of the contemporary scientists recognized it as an elementary substance, or studied it's properties in detail. Probably the first (al)chemist to study the properties of oxygen was C.W. Scheele. Scheele is reported to discover and identify many gases and elements, but he is not credited with the discovery of any of them. In his work on Air and Fire [2] the instructions on how to prepare oxygen are reported, but the publication was delayed until 1777 [3]. Three years earlier J. Priestley [4] had already published his method for the preparation of a colorless gas by heating mercury oxide. This gas would make a candle burn not only "*. . . with a remarkable vigorous flame . . .*" but also for a longer time when put in an enclosed space. According to theory at that time air could no longer support combustion or life when it became saturated with phlogiston, the compound believed to be released into the air during combustion [5]. He therefore called this unknown gas "*dephlogisticated air*".

It was due to his careful quantitative experimental work that Lavoisier noticed conservation of mass in chemical reactions and that combustion involved a reaction with oxygen. He proposed the oxygen theory of combustion and described it's role in oxidation and respiration [6]. After realizing that oxygen was an elemental gas it was Lavoisier who proposed the name oxygen from the Greek *oxys*, meaning sharp or acid and *genes*, meaning forming or generating [1, 6].

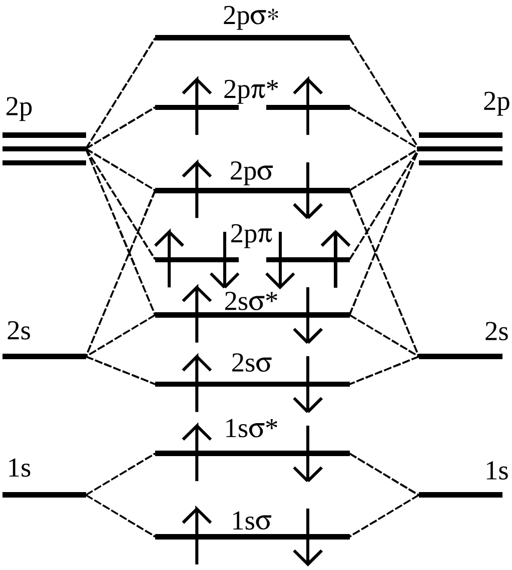

Figure 5.1: The energy level diagram of oxygen in which the interaction of the *2s* and *2p* atomic orbitals has been taken into account for the relative energies. The $S = 1$ state originates from the exchange interactions between the $2p\pi^*$ orbitals.

5.1.2 The ground state of molecular oxygen

Molecular oxygen at room temperature and ambient pressure is a colorless gas with an unusual bi-radical ground state due to the arrangement of the 16 electrons over the available molecular orbitals (fig. 5.1).

$$1s\sigma_g^2 \; 1s\sigma_u^{*2} \; 2s\sigma_g^2 \; 2s\sigma_u^{*2} \; 2p\pi_u^4 \; 2p\sigma_g^2 \; 2p\pi_g^{*2}$$

The subscripts g and u denote "*gerade*" or "*ungerade*" molecular orbitals. The superscript $*$ specifies that the corresponding electrons populate an anti-bonding molecular orbital. The unpaired $2p\pi_g^*$ electrons interact to form three symmetric ($\uparrow\uparrow$, $\downarrow\downarrow$ and $(\uparrow\downarrow + \downarrow\uparrow)$) and one antisymmetric ($\uparrow\downarrow - \downarrow\uparrow$) electronic state [7, page 220-224]. The relative energies of these states is determined by the amount and nature of the exchange

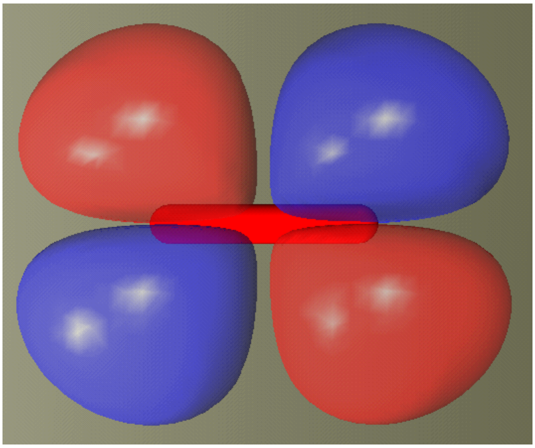

Figure 5.2: Visual representation of one of two the $2p\pi^*$ molecular orbitals. The oxygen atoms are located near the ends of the center bar. The antibonding orbital perpendicular to the one depicted here has no formal overlap with the shown orbital.

interaction (J). A positive value of J favors the symmetric states. The experimentally observed $S = 1$ state can be understood by applying Hund's rule of maximum multiplicity for molecules, as is normally done for atoms. The configuration with the two degenerate highest occupied orbitals gives rise to a $^3\sum$ ground state [8]. A second viewpoint explaining a triplet ground state stems from the analogy with orbital interaction in conjugated transition metal ions. A rule of thumb proposed by Goodenough and Kamamori states that the exchange interaction between orbitals of unpaired electrons, which have no formal overlap integral, but are arranged in such a way as to be in contact is positive [9, chapter 1]. The interacting $2p\pi^*$ molecular orbitals (fig. 5.2) have no formal overlap, but due to the small percentage of s-orbital they can be thought of as being in contact.

Spin-spin interactions cause a zero field splitting for the low lying electronic states. For gas phase molecular oxygen this zero field splitting (D), is reported to be 3.994 cm^{-1} [10]. The gas phase ground state can be adequately described by the simplified Hamiltonian 5.1 for an $S = 1$ system,

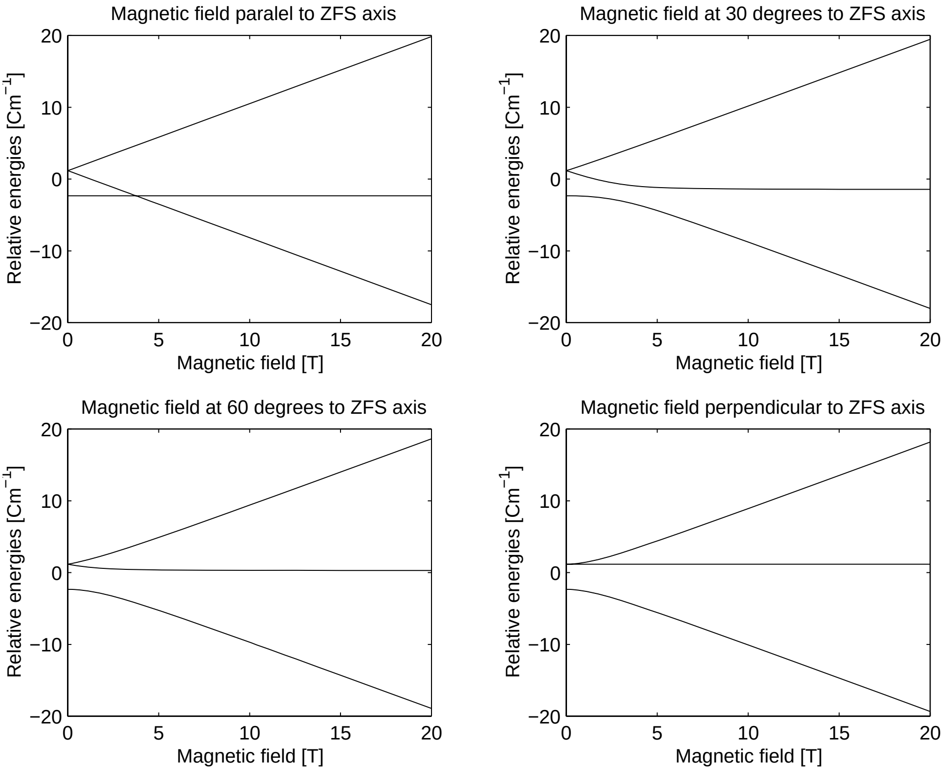

Magnetic field paralel to ZFS axis

Magnetic field at 30 degrees to ZFS axis

Magnetic field at 60 degrees to ZFS axis

Magnetic field perpendicular to ZFS axis

Figure 5.3: The relative energy of the symmetric electronic states for various magnetic field directions. The different orientations with respect to the magnetic field mixes the pure spin states and allow previously forbidden transitions. Calculations were based on $g_{iso} = 2.0023$ and $D = 3.994$ cm^{-1}.

disregarding the presence of the anti-symmetric energy level, rotational and vibrational terms [11, 12, 13, 14]:

$$\mathcal{H} = \mu_B \overrightarrow{B}\overline{\overline{g}}\overrightarrow{S} \ + \ D\left[S_z^2 - \frac{S(S+1)}{3}\right] \tag{5.1}$$

Oxygen liquefies at 90.2 K, into a paramagnetic fluid. Below 54.8 K oxygen solidifies in the first "*rotationally disordered (plastic)-phase*", or

γ-phase, a paramagnetic phase. At 43.6 K γ-oxygen undergoes an antiferromagnetic phase transition to β-oxygen, an antiferromagnetic solid. At 23.9 K a second antiferromagnetic phase transition changes the crystal structure from a *hR2* ($R\overline{3}m$) to *mC4* ($C2m$), characterized by a doubling of the antiferromagnetic lattice [1, 15]. It is speculated that the driving force behind this doubling is an extension from short range antiferromagnetic domains to a fully antiferromagnetic structure. As a result oxygen has a magnetic structure, resulting in spin wave dynamics. The molecular crystals have been studied quite well, as the review article of G.C. DeFotis shows [15]. The antiferromagnetic structure of pure molecular oxygen makes it difficult to determine the spin state of the oxygen molecules. Generally it is assumed that the spin state of oxygen molecules in the gas phase is also valid in the solid state and not influenced by the surroundings of the individual oxygen molecules. In order to reconcile the theoretical predictions better with the experimental data, preferred spin directions were assumed, resulting in long range quasi 1 and 2 dimensional structures [16, 17].

EPR-spectra in the magnetic field range of conventional EPR spectrometers have been reported for the liquid and γ-phase of pure molecular oxygen. The observed line broadening was believed to originate from intermolecular interactions, analogous to the long range interactions in the α and β phases. A decrease in line width was reported as the temperature was raised [18, 19, 20].

5.2 Contradicting indications

5.2.1 Pure molecular oxygen

β-Oxygen is antiferromagnetically ordered and has no net magnetization that can be correlated to individual molecules or moments. Measurements of both the magnetic susceptibility and the crystal structure demonstrated that the phase transition from β to α oxygen is accompanied by a discontinuous decrease in the magnetic susceptibility [21, 22]. Assuming a rigid anti-ferromagnetic ground state the β to α transition was attributed to an extension from short range ordering into long range ordering [23]. Only recently it was shown with the aid of Muon Spin Resonance (μSR) that at the antiferromagnetic $\beta \rightarrow \alpha$ transition a steplike increase of local magnetic moment of oxygen molecules from 0.8 to 1.5 Bohr magneton occurs [24], indicating that the triplet spin state of the oxygen molecule is not completely rigid.

5.2.2 Diluted molecular oxygen

Molecular oxygen can be diluted in a (diamagnetic) host lattice to minimize long range magnetic interactions. EPR measurements on such systems have been reported in the early 1950's [25]. It was not until 1970 that the first EPR spectra of molecular oxygen diluted in an inert gas host lattice was presented and discussed[1] [11]. These first experiments were performed at X- and K-band frequencies. Allowing only the nominally forbidden $\Delta\text{m} = 2$ transition. Consequently the reported values for D were varied (table 5.1).

Table 5.1: Reported g- and D-values for various hosts and temperatures. The D values have been converted to cm^{-1} for ease of comparison.

Matrix	g			D [cm^{-1}]	E [cm^{-1}]	T [K]	Ref
$NaClO_3$	2.004	2.006	2.003	3.743	0.33	4.2	[13]
$NaClO_3$	2.0049	2.0049	2.0022	3.742	0.131	4.2	[13]
$KClO_4$	2.0049	2.0049	2.0022	3.769	0.502	2.7	[13]
$KClO_4$	2.0047	2.0049	2.0023	3.468	1.985	–	[13]
$KBrO_4$	1.99	2.015	1.996	3.656	–	≈ 26	[12]
$KBrO_4$	1.98	2.01	2.01	3.636	–	≈ 26	[12]
N_2	2.0	2.0	2.0	3.612	–	< 20	[20]
N_2	2.0	2.0	2.0	3.572	–	4.2	[11]
N_2	2.0	2.0	2.0	3.572	–	16	[11]
N_2	2.02	2.02	2.02	3.602	–	< 20	[29]
N_2	2.000	2.000	2.000	3.572	–	5	[14]
CO	2.0	2.0	2.0	3.619	–	< 20	[20]
CO	2.02	2.02	2.02	3.602	–	< 20	[29]

---

[1] In contemporary textbooks frozen air is reported to account for dielectric losses in conventional EPR-spectrometers. Due to their relatively low frequencies no mention was made of the EPR signals that one could expect from the transitions in the triplet state of molecular oxygen [26, 27, 28].

Molecular oxygen is formed in certain crystals after irradiation with either photons or electrons and EPR spectra have been recorded of oxygen molecules in $NaClO_3$, $KClO_4$, LiO_2 and amorphous aluminum borates [12, 13, 30, 31]. The reported g-values for the different matrices are nearly identical, despite the different lattice sites in the various hosts (table 5.1).

The EPR data of diluted molecular oxygen have been reported for temperatures up to about 25 K (table 5.1) and upwards of 60 K [18, 19]. The $S = 1$ signal is reported to broaden when the temperature is raised, becoming undetectable above approximately 25 K [10, 20, 29].

5.3 Experimental set-up

The present experiments were performed with the set-up described in section 2.4. The desired oxygen concentrations were prepared by mixing the appropriate partial pressures of oxygen and the host gas in a 0.5 L lecture bottle. Transfer to the sample holder was by means of a small capillary in the waveguide. Two procedures were used to condense the gas-mixture in the sample holder:

1. The flow cryostat was stabilized at a temperature of 70 K at which both gases would liquefy in the sample holder. After allowing the gas some time to collect in the sample holder the temperature was lowered to the desired experimental temperature.

2. The flow cryostat was cooled down to about 10 K. The low temperature results in a near instant solidification when the gas mixture comes in contact with the sample holder. In order to prevent heating of the sample holder the gas mixture was added in small amounts. Afterwards the temperature was raised to the desired experimental temperature.

The first procedure gives the best results for mixtures where the liquefied gases mix, as is the case for oxygen and nitrogen. If the two gases separate in the liquid phase, such as appears to be the case for oxygen and argon, the second procedure is better since the fast solidification prevents phase separation.

The dilution of oxygen in carbon dioxide did not yield an $S = 1$ resonance at low temperatures, regardless of the concentration. Probably the difference between the high sublimation point of carbon dioxide (195 K), and the boiling point of oxygen (90 K) results in phase separation.

5.4 Experimental determination of the low temperature ground state of molecular oxygen by HF-EPR

5.4.1 Determination of the zero field splitting

EPR spectra were recorded for various concentrations of oxygen in a nitrogen matrix at frequencies ranging from 80 to 380 GHz. Special attention was paid to the range 80 to 120 GHz. All measurements performed at oxygen concentrations of 0.4, 4 and 20 % could be fitted with Hamiltonian 5.1 for an $S = 1$ system assuming a random distribution. In the loading process

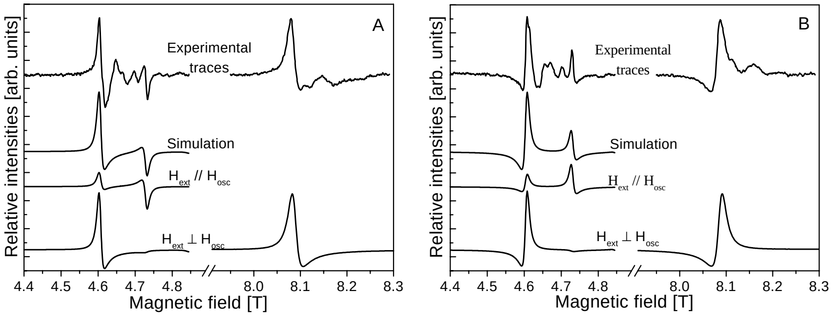

Figure 5.4: The real (A) and imaginary part (B) of a typical EPR resonance of O_2 diluted in an N_2 matrix at 15 K compared with simulations based on $S = 1$, $g_{iso} = 2.0023$ and $D = 3.497\ \mathrm{cm}^{-1}$. Due to the occurrences of both parallel and perpendicular excitations both processes have to be combined for an accurate fit at low field. At high magnetic field the intensity of the parallel transition is negligible.

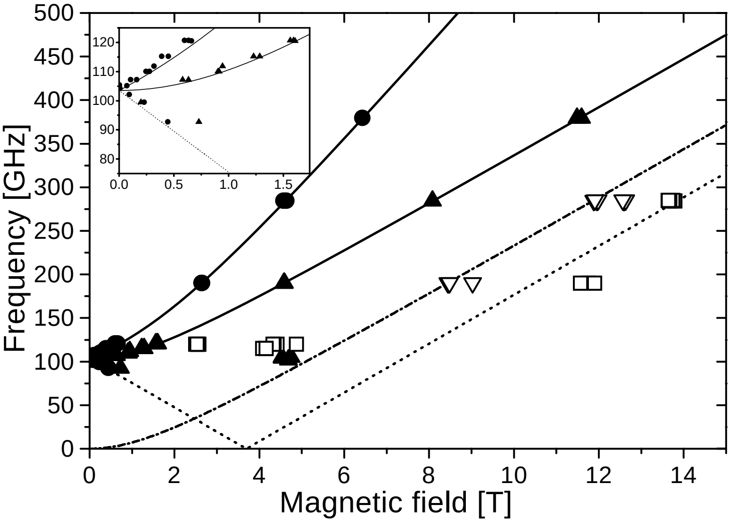

Figure 5.5: Resonance positions of oxygen EPR spectra in a nitrogen matrix at 15 K. The drawn lines are theoretical values based on $S = 1$, $g_{iso} = 2.0023$ and $D = 3.497$ cm^{-1}.

the location where the gas mixture solidifies is not under full control. Most of the EPR active centers will condense on the bottom of the non-resonant sample holder, but a small part will solidify in an area where the external and oscillating magnetic fields are parallel. Although this is usually a weak transition, becoming even weaker at high magnetic fields, it is sufficiently present to need both perpendicular and parallel EPR transitions for a good fit (fig. 5.4). The resonance at 12 T was weak at 15 K temperature and became unobservable at higher temperatures. At concentrations of 50 and 80 % oxygen no EPR signal could be detected. Presumably oxygen forms antiferromagnetic domains at these concentrations which are EPR silent. The observed g_{iso} of 2.0023 is in agreement with both gas phase measurements and theory [32, 33, 34]. The zero field splitting at 15 K was determined to be 3.497 cm^{-1}, without rhombicity.

The zero field splitting was determined by two independent methods: observation of the direct microwave transition at zero magnetic field and a fit through the resonance frequencies against the magnetic field value (fig. 5.5). Filled and open markers represent high and low intensity resonances respectively. The drawn lines are the theoretical values based on $S = 1$, $g_{iso} = 2.0023$ and $D = 3.497$ cm^{-1}. Experiments on a 10 % concentration of oxygen in an argon host yielded nearly identical parameters at low temperatures. Overall there is good agreement between experimental results and the theoretical description. Despite the unambiguous assignment of D in this type of experiment it differs remarkably from the 3.572(3) cm^{-1} reported by Pardi and coworkers, who employed a similar approach to determine D in solid air at 5 K [14], in the following section an explanation is proposed for this discrepancy.

5.4.2 Temperature dependence of the $S = 1$ resonances

The temperature dependence was studied in the range 15 to 50 K. Typical low temperature spectra are shown in figure 5.6. Two effects of the temperature are a shift of the observed resonances to higher magnetic field values and a simultaneous decrease of the observed intensity (or more correctly the observed height of the first derivative of the signal) and weak line broadening with increasing temperature. Both resonances become undetectable near 25 K.

Shift to higher magnetic field values

The temperature dependent field shift indicates a reduced D. The decrease of D becomes more pronounced at higher temperatures, independent of the oxygen concentration (fig. 5.7). The temperature dependence of the zero field splitting reflects a changing sensitivity to the environment. To exclude a matrix effect the same data has been collected on oxygen diluted in an argon matrix. Here the same temperature dependence can be seen, but is more pronounced (fig. 5.8).

Temperature dependent changes of D for molecular oxygen in a host lattice have been reported before and were attributed to hindered librational motion in the host crystal lattice. The librational motion was thought to couple to the spin state by means of off-diagonal matrix elements [10, 13, 34]. For small corrections to the resonance position this coupling is suffi-

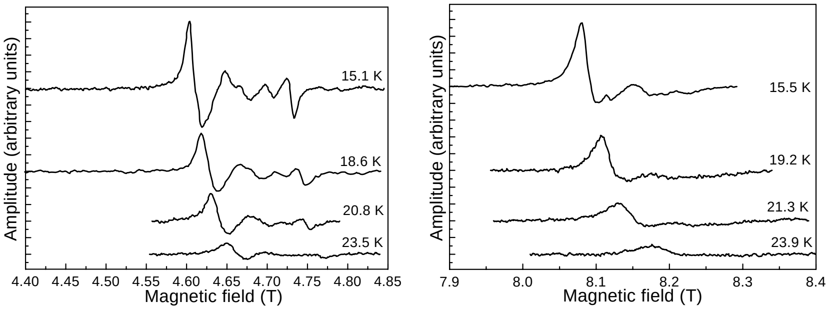

Figure 5.6: The temperature dependence of the two observable resonances of oxygen in a solid nitrogen host at 285 GHz. The shift to higher field values and the decreased height in combination with line broadening are visible. Only the trace corresponding to the first derivative of the real part of the resonance is plotted.

cient, but it is stretched to its limit to explain the relatively large shift in D near 25 K. The proposed population of higher order librational modes fails for high frequency experiments. The proposed zero field splitting of the first excited librational state is about 3.1 cm^{-1} which is low enough to be observable as an individual signal alongside the signal of the ground state librational motion in the 285 GHz spectra, which did not show in any of the EPR spectra we recorded. [10, 34]. Furthermore it would be field independent, while the observed behaviour is field dependent.

Disappearance of the $S = 1$ signal

Previously the decrease in intensity of the $S = 1$ transitions was attributed to line broadening [13, 29], which indeed occurs simultaneously with a decrease in amplitude. The line widths obtained in fitting the data are plotted in figure 5.9 showing a strong increase between 15 and 25 K. However, the maximum line width observed at 25 K is only 70 mT, which for HF-EPR is not particularly broad and cannot be responsible for the disappearing of the $S = 1$ signal above 25 K.

The integrated intensity of an optical transition is proportional to the

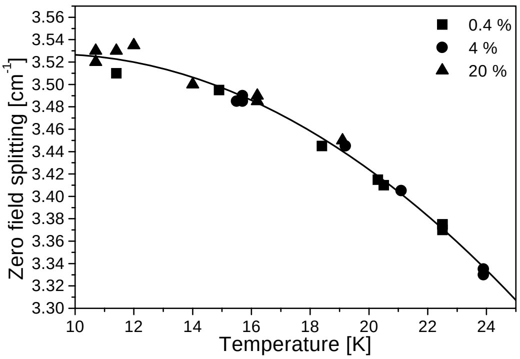

Figure 5.7: The decrease of D with temperature for molecular oxygen in a nitrogen matrix. The concentration of oxygen does not appear to have a significant influence. Above 25 K no $S = 1$ signal could be detected.

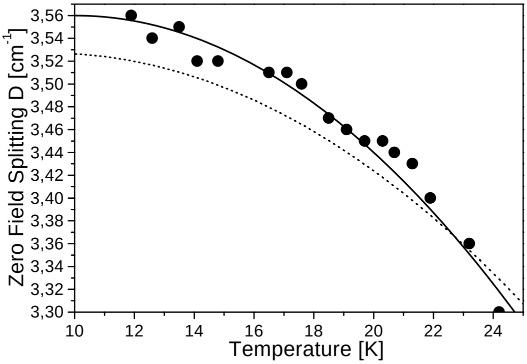

Figure 5.8: Temperature dependence of the zero field splitting of a 10 % concentration of molecular oxygen in an argon host lattice. The dotted line is the temperature dependence of the zero field splitting of oxygen in a nitrogen host, reproduced from figure 5.7.

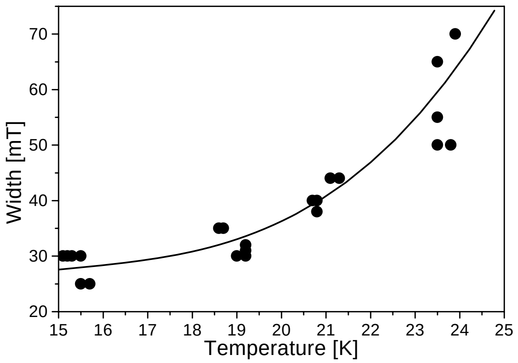

Figure 5.9: Temperature dependent line width for good fit. Plotted are the line widths for a 4 % oxygen concentration. The drawn line is an exponential function to guide the eye.

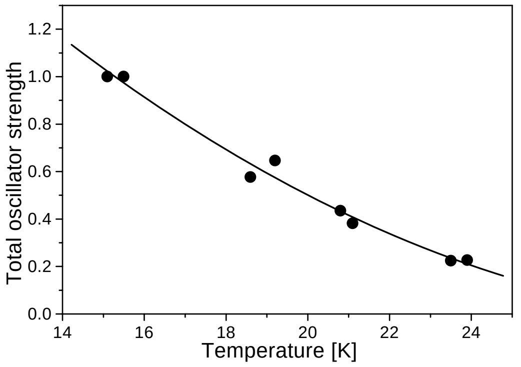

Figure 5.10: Corrected total oscillator strengths for triplet molecular oxygen in a nitrogen host lattice. The signal strength observed at 15 K is normalized to 1. The strong decrease identifies the reduction of observed signal strength as a disappearance of the $S = 1$ states.

number of oscillators present in the system. The number of participating oscillators can therefore be determined by calculating the double integral of the recorded first derivative spectra [26, p. 591]. A change in intensity is expected by the temperature dependence of the zero field splitting which affects the thermal occupation of the energy levels because of the change in energy, but this is too small and cannot account for it. Furthermore this is an effect that can be corrected for. The total oscillator strengths after correction for various temperatures are plotted in figure 5.10. Clearly it can be seen that increasing temperatures cause a decrease in the total oscillator strength, which indicates the loss of molecular oxygen in a triplet spin state.

Observation of a quasi-continuum at $g \approx 2$ for $S = \frac{1}{2}$

At low temperatures $S = 1$ transitions could readily be detected in direct detection (no field modulation), but surprisingly they are super-imposed on

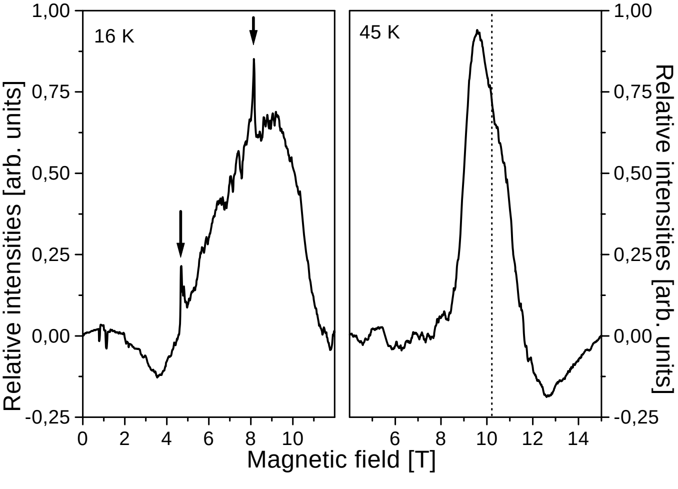

Figure 5.11: Direct detection of the EPR transitions of molecular oxygen in a nitrogen host at 285 GHz. The expected $S = 1$ transitions at low temperature are marked with arrows. In the high temperature spectrum the expected position for a $g = 2.0$, $S = \frac{1}{2}$ resonance is marked by the dotted line.

a very broad quasi-continuum (fig. 5.11) which is independent of concentration. In literature no mention is made of the existence of such a quasi-continuum. In order to check for contamination different sample holders were prepared, and it was verified that the quasi-continuum is only present after loading. On the basis of the available number of spins for the lowest concentration of oxygen (0.4 %) approximately $5.4{\cdot}10^{18}$ spins are present in the set-up. This value lies well within the detection limit of the non-resonant EPR-set-up (see section 2.4.3) and leads us to believe that oxygen is the source of this broad signal. The quasi-continuum prevails at the intermediate temperatures where the $S = 1$ resonances are unobservable. Furthermore at increasing temperatures the quasi-continuum narrows down considerably, ranging from a full width at half maximum of 5 tesla at 15 K to about 2 tesla at 45 K. At 45 K it is located slightly below the expected magnetic field value for an $S = \frac{1}{2}$ system with $g_{iso} = 2.0$ at 285 GHz. We therefore belief that the broad continuum is caused by an $S = \frac{1}{2}$ species with very strong interactions.

5.5 Discussion

The spin triplet state of molecular oxygen in the solid state was always assumed to be rigid. Small variations of D with respect to the gas phase value of 3.994 cm^{-1} were attributed to the imperfect crystal structure of the host lattice. For molecular oxygen in the gas phase the assumption of an unperturbed (rigid) ground state still appears to be correct. As soon as the oxygen molecules interact with a host lattice in a condensed phase observations can be made that invalidate the assumption of a rigid ground state.

5.5.1 Measurements on pure molecular oxygen

Measurements of the EPR spectra of molecular oxygen in the gas phase have been the foundation of the magnetic ground state. In the gas phase the oxygen molecules are not disturbed by the presence of interactions resulting in the measurement of the "*pure*" ground state. Microwave magnetic experiments at elevated temperatures show different rotationally excited signals,

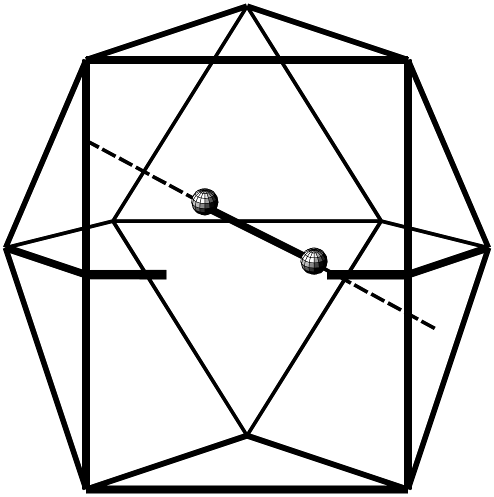

Figure 5.12: Oxygen molecule shown within a cage modeled on the hcp lattice of solid nitrogen, reproduced from [37]. The nodes of the cage are the centers of mass of the surrounding molecules. The arrangement of triangular and square faces in the cage results in three positions of minimum interaction.

but both the zero field splitting (D) and the isotropic g-value remain constant [25, 35, 36].

The EPR spectrum of oxygen in the liquid phase, as observed by others and ourself, is remarkably different [18, 19, 20]. Very broad resonances are observed. Originally this extreme broadening was attributed to interactions between the triplet states, but in our own experiments the same behaviour was observed when oxygen was diluted in nitrogen to a concentration of 1 in 200 molecules.

5.5.2 Oxygen diluted in a host matrix

The rotational/vibrational (= librational) motion of the oxygen molecule in a solid host can be envisioned as a barbel in a cage. For oxygen in a nitrogen host this has been visualized in figure 5.12. Since the relative sizes of oxygen and nitrogen differ by only 2% [38, 39] it can be safely assumed that oxygen replaces nitrogen in the crystal structure. Oxygen is reported to start a librational motion at temperatures of about 10 K [40]. Extrapolation from figures 5.7 and 5.8 show that the zero field splitting starts to decrease noticeably from this temperature, indicating a dependence of the zero field splitting on the temperature. The nitrogen molecules on the other hand are restricted in their librational motion until 35 K [41], while Argon only has one solid state. This rules out that the observed effects on the oxygen EPR spectra are due to a disturbance of the host lattice.

5.6 Conclusion

The disappearance of the $S = 1$ signal of molecular oxygen diluted in a diamagnetic host, combined with the strong reduction of the zero field splitting at elevated temperatures indicates a breakdown of the triplet ground state of molecular oxygen. Direct detection methods revealed that at relatively low temperatures an additional EPR signal can be detected which spans several tesla. This broad quasi-continuum persists at temperatures where the $S = 1$ signal cannot be measured and narrows at higher temperatures. The center of the quasi-continuum is located slightly below the $g = 2.0$ position for an $S = \frac{1}{2}$ system. It is proposed that the interaction of the oxygen molecule with the environment perturbs the ground state in a way that allows the two unpaired electrons in the antibonding orbitals to interact, but not sufficient to couple into an $S = 1$ state. The resulting ground state being two interacting, but essentially incoherent, $S = \frac{1}{2}$ spins on the same oxygen molecule. This perturbation of the ground-state might also explain some of the observations reported using other spectroscopic studies. The transformation of the ground state is consistent with the data observed on the local magnetic moment of pure oxygen at the $\alpha \rightarrow \beta$ transition temperature.

Bibliography

[1] D.R. Lide (*editor in chief*). *Handbook of Chemistry and Physics, 72nd special student edition.* The Chemical Rubber Company, 1991.

[2] Encyclopedia Brittanica. Scheele, Carl Wilhelm. WWW.Brittanica.com, 1999-2000.

[3] C.W. Scheele. *Chemische abhandlung von der luft und dem feuer.* W. Engelman, 1777.

[4] Encyclopedia Brittanica. Priestley, Joseph. WWW.Brittanica.com, 1999-2000.

[5] Encyclopedia Brittanica. Phlogiston. WWW.Brittanica.com, 1999-2000.

[6] Encyclopedia Brittanica. Lavoisier, Antoine-Laurant. WWW.Brittanica.com, 1999-2000.

[7] D. Craik. *Magnetism, principles and apllications.* John Wiley & sons, 1995.

[8] P.W. Atkins. *Molecular Quantum Mechanics.* Oxford University Press, 1983.

[9] A. Bencini and D. Gatteschi. *EPR of exchange coupled systems.* Springer-Verlag, 1990.

[10] S. Hirokawa. Theory of the electron paramagnetic resonance of oxygen impurity in solid nitrogen. *J. Phys. Soc. Jap.*, 35:12–17, 1973.

[11] G.M. Graham, J.S.M. Harvey, and H. Kiefte. EPR of O_2 impurity in solid N_2. *J. Chem. Phys*, 52:2235–2237, 1970.

[12] J.R. Byberg. Detection by ESR of oxygen molecules formed as defects in single crystals. *Chem. Phys. Lett.*, 57:579–581, 1978.

[13] N. Bjerre. ESR study of the librations of O_2 defects in $NaClO_3$ and $KClO_4$ single crystals. *J. Chem. Phys.*, 76:3347–3351, 1982.

[14] L.A. Pardi, J. Krystek, J. Teller, and L.C. Brunel. Multifrequency EPR spectra of molecular oxygen solid air. *J. Magn. Reson.*, 146:375–378, 2000.

[15] G.C. DeFotis. Transformation characteristics and orientation relations among the phases of solid oxygen. *J. Chem. Phys.*, 71:5336–5351, 1979.

[16] A.P.J. Jansen. *Theoretical approach to the Optical, Thermodynamic and Magnetic Properties of Solid Nitrogen and Solid Oxygen.* PhD thesis, University of Nijmegen, 1987.

[17] A. de Bernabe, G.J. Cuello, F.J. Bermeo, F.R. Trouw, and A.P.J. Janssen. Vibrational dynamics in solid α-oxygen: Experimental assesment of spin-phonon couplings. *Phys. Rev. B.*, 58:14442–14451, 1998.

[18] E.P. Yudin. Temperature dependence of the electron paramagnetic resonance spectrum of liquid oxygen. *JETP Lett.*, 27:120–122, 1978.

[19] E.P. Yudin. Electron paramagnetic resonance of γ-oxygen. *JETP Lett.*, 26:344–346, 1977.

[20] H. Kon. Paramagnetic resonance of molecular oxygen in condensed phases. *J. Am. Chem. Soc.*, 95:1045–1049, 1973.

[21] G.C. DeFotis. Magnetism of solid oxygen. *Phys. Rev. B.*, 23:4717–4740, 1981.

[22] D.E. Cox, E.J. Samuelsen, and K.H. Beckurts. Neutron-diffraction determination of the crystal structure and magnetic form factor of γ-oxygen. *Phys. Rev. B*, 7:3102–3111, 1973.

[23] A.J.R. da Silva and L.M. Falicov. Magnetism and the $\alpha - \beta$ phase transition in solid oxygen. *Chem. Phys. Lett.*, 222:339–342, 1994.

[24] F.J. Bermeo, A. de Bernabé, J.L. Martínez, M.L. Senent, G.J. Guello, S.F.J. Cox, F. Dunstetter, and F. Trouw. Magnetic dynamics in condensed oxygen: recent experimental results. *J. Low. Temp. Phys.*, 111:287–302, 1998.

[25] R. Beringer and J.G. Castle. Microwave magnetic resonance spectrum of oxygen. *Phys. Rev.*, 81:82–88, 1951.

[26] C.P. Poole. *Electron Spin Resonance, a comprehensive treatise on experimental techniques.* John Wiley & sons, 1967.

[27] J.W. Orton. *Electron Paramagnetic Resonance, an introduction to transition group ions in crystals.* London Ilife Books LTD, 1968.

[28] A. Abragam and B. Bleaney. *Electron Paramagnetic Resonance of Transition Ions.* Clarendon Press, Oxford, 1970.

[29] R. Simoneau, J.S.M. Harvey, and G.M. Graham. EPR of O_2 impurity in solid N_2, CO, Ar and CD_4 prepared from the vapor. *J. Chem. Phys.*, 54:4819–4824, 1971.

[30] S. Simon, A. van der Pol, E.J. Reijerse, A.P.M. Kentgens, G.J. van Moorsel, and E. de Boer. EPR and NMR studies of amorphous aluminium borates. *Chem. Soc. Faraday Trans.*, 90:2663–2670, 1994.

[31] F. Beuneu, P. Vadja, and O.J. Zogal. Evidence of molecular-oxygen inclusion in electron-irridiated Li_2O crystals through magnetization measurements. *Phys. Rev, Lett.*, 83:761–763, 1999.

[32] M. Tinkham and M.W.P. Strandberg. Interaction of molecular oxygen with a magnetic field. *Phys. Rev.*, 97:951–966, 1955.

[33] M. Tinkham and M.W.P. Strandberg. Theory of the fine structure of the molecular oxygen ground state. *Phys. Rev.*, 97:937–951, 1955.

[34] S. Hirokawa. Theory of polycrystalline electron paramagnetic resonance spectra of the oxygen molecule in librational motion. *J. Phys. Soc. Jap*, 37:897–903, 1974.

[35] T.J. Cook, B.R. Zegarski, H. Breckenridge, and T.A. Miller. Gas phase EPR of vibrationally excited O_2. *J. Chem. Phys.*, 58:1548–1552, 1973.

[36] P. Gerber. Hyperfeinstruktur des elektronenspinresonanzspektrums von molekularem sauerstoff in der gasphase. *Helv. Phys. Acta.*, 45:655–682, 1972.

[37] W.E. Streib, T.H. Jordan, and W.N. Lipscomb. Single-Crystal X-ray diffraction study of β-nitrogen. *J. Chem. Phys.*, 37:2962–2965, 1962.

[38] T.H. Jordan, H.W. Smith, W.E. Streib, and W.N. Lipscomb. Single-Crystal diffraction studies of α-N_2 and β-N_2. *J. Chem. Phys.*, 41:756–759, 1964.

[39] K. Schou Pedersen and F. Yssing Hansen. Thermal neutron diffraction from the liquids N_2 and O_2. determination of the nearest neighbor parameters and angular correlations. *J. Chem. Phys.*, 70:1051–1055, 1979.

[40] C. Uyeda, K. Sugiyama, and M. Date. High field magnetization of solid oxygen. *J. Phys. Soc. Jap*, 54:1107–1115, 1985.

[41] A. Mulder, J.P.J. Michels, and J.A. Schouten. Monte carlo simulations of the $\gamma - \beta$, $\alpha - \gamma$ and $\alpha - \beta$ phase transitions of nitrogen. *J. Chem. Phys.*, 106:8806–8813, 1997.

Summary

Electron Paramagnetic Resonance (EPR) is a technique that is intrinsically limited to unpaired electron spins in various matrices. Traditionally the frequencies at which EPR set-ups operated were limited (9, 22, 35 and recently 95 GHz). Current state of the art set-ups operate at frequencies of 130 GHz or above. The benefits of EPR operation at high frequencies are the increased g-tensor resolution and the ability to measure spins systems with a large zero field splitting (D). Theoretically an increase of the sensitivity is predicted, but due to restrictions on resonator and sample size the effect is limited. Ease of use is improved by employing non-resonant and/or oversized techniques, at the expense of sensitivity.

Using HF-EPR data in combination with other techniques the ground state and/or the presence of a magnetic phase transition in a number of spin systems with unusual properties have been studied.

Multifrequency EPR measurements on Ni^{2+} ions both above and below the crystallographic phase transition temperature of the $Zn(en)_3(NO_3)_2$ host indicated that the additional resonance alongside the $S = 1$ multiplet of the Ni^{2+} ions did not originate from the alleged double quantum resonance. The most probable cause for the observed resonance was the presence of an $S = \frac{3}{2}$ impurity. Theoretical predictions of how an $S = \frac{3}{2}$ impurity would behave when enclosed in the $Zn(en)_3(NO_3)_2$ host matrix were in good agreement with the results observed.

Pure $Mn(C_5H_5)_2$ is a salt with an elusive ground state. Theoretically the Mn^{2+} ions can exist in a low spin ($S = \frac{1}{2}$) or a high spin ($S = \frac{5}{2}$) state. In diluted specimens both spin states and equilibria between the two states have been detected. By combining multifrequency EPR measurements of the powdered solid at various temperatures with data obtained from mag-

netization measurements we determined the ground state to be $S = \frac{5}{2}$. Due to magnetic interactions an additional resonance is observed alongside the $S = \frac{5}{2}$ resonance. By deduction this signal is attributed to the antiferromagnetic resonance of the quasi 1-dimensional chains that exist within the solid. At low magnetic fields and temperatures this is the predominant signal observed in an EPR spectrum.

The ground state of solid molecular oxygen was assumed to be a rigid $S = 1$ spin system. EPR measurements on molecular oxygen at various concentrations in host matrices indicated that the $S = 1$ spin system is not rigid. In the lowest temperature region the $S = 1$ spins exhibit a sharp decrease of the total intensity and the zero field splitting value upon approaching 25 K. Simultaneously a very broad resonance was observed at $g \approx 2$ for an $S = \frac{1}{2}$ spin system. The broad quasi-continuum could be observed up to the melting point of the host matrices. Combining the experimental data with data from literature led to the conclusion that the ground state of molecular oxygen is susceptible to changes. Under certain conditions the $S = 1$ spin state is disrupted. The resulting $S = \frac{1}{2}$ spinstates are exchange broadened due to their close proximity.

The number of systems where EPR can be used in determining ground state properties of materials are few. The data (HF)-EPR can yield, especially when combined with data from other sources, give a unique insight in the (para) magnetic state of materials. An insight that other techniques cannot provide. Therefore the current development of HF-EPR systems, in tandem with other high field techniques is fully justified.

Samenvatting

Electron Paramagnetische Resonantie (EPR) is een techniek die intrinsiek gelimiteerd is tot systemen van ongepaarde electron spins binnen verschillende matrices. Traditioneel zijn de frequenties altijd beperkt geweest (9, 22, 35 en recentelijk 95 GHz). De huidige generatie apparatuur werkt met frequenties van 130 GHz en hoger. De voordelen van EPR bij hogere frequenties zijn de verbeterde g-tensor resolutie en de mogelijkheid om spin systemen te meten met een grote nulveld splitsing. Theoretisch wordt ook een verhoging van de gevoeligheid voorspeld, maar restricties aan de resonator en monstergrootte limiteren dat effect. Gebruiksgemak wordt verkregen door gebruik te maken van niet-resonante of oversized technieken, ten koste van een lagere gevoeligheid. Door gebruik te maken van HF-EPR data in combinatie met andere technieken is de grond-toestand en/of de aanwezigheid van magnetische fase overgangen in een aantal spin systemen met ongewone eigenschappen bestudeerd.

Multifrequente EPR metingen aan Ni^{2+} ionen zowel boven als onder de crystallografische fase overgangstemperatuur van een $\mathrm{Zn(en)_3(NO_3)_2}$ matrix tonen aan dat het extra signaal naast het $S = 1$ multiplet niet afkomstig is van een dubbel quantum resonantie. De meest waarschijnlijke oorzaak van de geobserveerde resonantie was de aanwezigheid van een $S = \frac{3}{2}$ verontreiniging. Theoretische voorspellingen over hoe een $S = \frac{3}{2}$ verontreiniging zich gedraagt in de $\mathrm{Zn(en)_3(NO_3)_2}$ matrix laten goede overeenkomsten zien met de geobserveerde resultaten.

Zuiver $\mathrm{Mn(C_5H_5)_2}$ is een zout met een moeilijk te bepalen grondtoestand. Theoretisch kunnen de Mn^{2+} ionen voorkomen in een laag- ($S = \frac{1}{2}$) en een hoog-spin ($S = \frac{5}{2}$) configuratie. In verdunde toestand zijn beide configuraties, en evenwichten tussen beide aangetroffen. Door multifrequente

EPR metingen aan verpoederd $Mn(C_5H_5)_2$ op verscheidene temperaturen te combineren met magnetisatie metingen is de grondtoestand bepaald als zijnde $S = \frac{5}{2}$. Door magnetische interacties wordt een tweede signaal naast de $S = \frac{5}{2}$ resonantie waargenomen. Door deductie is dit signaal toegewezen aan de antiferromagnetische resonantie van de quasi 1-dimensionale ketens die bestaan binnen de vaste stof. Op lage magnetische velden en temperaturen is de antiferromagnetische resonatie het belangrijkste signaal binnen een EPR spectrum.

Van de grondtoestand van vast moleculair zuurstof werd altijd aangenomen dat het een rigide $S = 1$ systeem was. EPR metingen aan moleculair zuurstof in verschillende concentraties en matrices geven aan dat het $S = 1$ spin systeem niet rigide is. In het laagste temperatuurgebied is een scherpe daling te zien van de totale intensiteit en de nulveld splitsing bij het bereiken van 25 K. Tegelijkertijd kan een breed quasi continuüm worden geobserveerd bij $g \approx 2$ voor een $S = \frac{1}{2}$ spin systeem. Dit quasi continuüm bleef zichtbaar tot aan het smeltpunt van de host matrices. Het combineren van de experimentele data met literatuur gegevens leidde ons tot de conclusie dat de grondtoestand van moleculair zuurstof in een matrix beïnvloed word. De resulterende $S = \frac{1}{2}$ spin toestanden zijn exchange verbreed door hun onderlinge nabijheid.

Het aantal materialen waar EPR gebruikt kan worden om de grondtoestand te achterhalen is beperkt. De gegevens die (HF-)EPR kan leveren, vooral gecombineerd met gegevens van andere bronnen, geven een uniek inzicht in de (para)magnetische grondtoestand van materialen. Daarom is de huidige ontwikkeling van HF-EPR systemen, volledig terecht.

Curriculum Vitae

Eric van der Horst is op 21 juni 1974 geboren in Amsterdam. In 1992 slaagde hij voor het VWO examen (Atheneum β) aan het Mondriaan lyceum. Aansluitend begon hij een studie scheikunde aan de Universtiteit van Amsterdam. Het propadeutisch examen werd in 1993 gehaald. Het doctoraal examen werd in 1996 afgelegd met als hoofdvak Massaspectrometrie bij Prof. dr. N.M.M. Nibbering. Hierna was een verhuizing naar Nijmegen noodzakelijk om bij de vakgroep Experimentele Vaste Stof Fysica (I) van Prof. dr. ir. J.C. Maan als AIO te werken in het Nijmeegs laboratorium voor hoge magneet velden. De resultaten van dat werk zijn uitgewerkt in dit proefschrift.

De huidige dienstbetrekking is Technical Specialist op het bio-analytisch laboratorium van Pharma Bio-Research in Assen.